



Published in final edited form as:

Cancer Discov. 2020 November ; 10(11): 1722–1741. doi:10.1158/2159-8290.CD-20-0160.

The Meningioma Enhancer Landscape Delineates Novel Subgroups and Drives Druggable Dependencies

Briana C. Prager^{1,2,3,4}, Harish N. Vasudevan⁵, Deobrat Dixit^{1,2}, Jean A. Bernatchez^{6,7}, Qiulian Wu^{1,2}, Lisa C. Wallace⁸, Shruti Bhargava^{1,2}, Derrick Lee^{1,2,9}, Bradley H. King^{1,2,9}, Andrew R. Morton⁴, Ryan C. Gimple^{1,2,4}, Melike Pekmezci¹⁷, Zhe Zhu¹, Jair L. Siqueira-Neto^{6,7}, Xiuxing Wang^{1,2,10}, Qi Xie^{1,2,11}, Clark Chen¹², Gene H. Barnett^{13,3}, Michael A. Vogelbaum^{13,14}, Stephen C. Mack¹⁵, Lukas Chavez¹⁶, Arie Perry¹⁷, David R. Raleigh^{5,18}, Jeremy N. Rich^{1,2,19}

¹Division of Regenerative Medicine, Department of Medicine, University of California, San Diego, La Jolla, CA, 92037, USA

²Sanford Consortium for Regenerative Medicine, La Jolla, CA 92037, USA

³Cleveland Clinic Lerner College of Medicine, Cleveland Clinic, Cleveland, OH, 44195, USA

⁴Case Western Reserve University Medical Scientist Training Program, Case Western Reserve University School of Medicine, Cleveland, OH, 44106, USA

⁵Department of Radiation Oncology, University of California, San Francisco, San Francisco, CA, 94143, USA

⁶Skaggs School of Pharmacy and Pharmaceutical Sciences, University of California, San Diego, La Jolla, CA, 92093, USA

⁷Center for Discovery and Innovation in Parasitic Diseases, University of California, San Diego, La Jolla, CA, 92093, USA

⁸Department of Biomedical Engineering, Cleveland Clinic, Cleveland, OH, 44195, USA

⁹University of California San Diego School of Medicine, University of California, San Diego, La Jolla, CA, 92093, USA

¹⁰School of Basic Medical Sciences, Nanjing Medical University, Nanjing, 211166, China

¹¹Institute of Basic Medical Sciences, Westlake Institute for Advanced Study, Westlake University, Hangzhou, 310000, China

¹²Department of Neurosurgery, University of Minnesota, Minneapolis, Minnesota, 55455, USA

¹³Department of Neurosurgery, Cleveland Clinic, Cleveland, OH, 44195, USA

Correspondence to: Jeremy N. Rich, 2880 Torrey Pines Scenic Drive, La Jolla, CA 92037, drjeremyrich@gmail.com, Phone: (858) 246-1208 or David R. Raleigh, University of California, San Francisco, 505 Parnassus Avenue, Room L-008, San Francisco, CA 94143, David.Raleigh@ucsf.edu, Phone: (415) 353-8950, Fax: (415) 353-8679.

Conflict of interest: The authors declare no potential conflicts of interest.

Data availability

All data has been deposited and can be downloaded using the SRA accession PRJNA579990 (WES) or GEO accession GSE139652 (ChIP-seq and RNA-seq).

14. Department of NeuroOncology, Moffitt Cancer Center, Tampa, FL, 33612, USA
15. Baylor College of Medicine, Houston, TX, 77030, USA
16. Department of Medicine, University of California, San Diego, San Diego, CA, 92037, USA
17. Department of Pathology, University of California, San Francisco, San Francisco, CA, 94143, USA
18. Department of Neurological Surgery, University of California, San Francisco, San Francisco, CA, 94143, USA
19. Department of Neurosciences, University of California, San Diego, La Jolla, CA, 92037, USA

Abstract

Meningiomas are the most common primary intracranial tumor with current classification offering limited therapeutic guidance. Here, we interrogated meningioma enhancer landscapes from 33 tumors to stratify patients based upon prognosis and identify novel meningioma-specific dependencies. Enhancers robustly stratified meningiomas into three biologically distinct groups (adipogenesis/cholesterol, mesodermal and neural crest) distinguished by distinct hormonal lineage transcriptional regulators. Meningioma landscapes clustered with intrinsic brain tumors and hormonally-responsive systemic cancers with meningioma subgroups reflecting progesterone or androgen hormonal signaling. Enhancer classification identified a subset of tumors with poor prognosis, irrespective of histological grading. Super enhancer signatures predicted drug dependencies with superior *in vitro* efficacy to treatment based upon the NF2 genomic profile. Inhibition of DUSP1, a novel and druggable meningioma target, impaired tumor growth *in vivo*. Collectively, epigenetic landscapes empower meningioma classification and identification of novel therapies.

Keywords

Meningioma; enhancers; epigenetics; brain tumors; progesterone signaling

INTRODUCTION

Meningiomas are the most common primary intracranial tumor, constituting over one-third of all primary central nervous system neoplasms (1). Meningiomas are classified by grade according to histologic characteristics; while most have been considered benign (WHO grade I), a substantial percentage are higher grade (WHO grades II and III) (1,2). Furthermore, histological grade fails to fully predict recurrence, and, upon failure of surgery and/or radiation, there are no effective systemic therapies for these patients.

Meningiomas exhibit a very strong and unexplained epidemiological sex bias. Grade I tumors afflict female over male patients at a 3:1 ratio, a predilection that is lost in higher grade tumors (1). Case reports and small studies have implicated progesterone agonists in meningioma growth, with reports of tumor regression following discontinuation of exogenous progesterone (3,4). However, clinical trials have demonstrated inconsistent results and predicting responders to hormone therapy remains a significant challenge (5-8).

Identifying the basis for heterogeneity of hormonal responsiveness and the role of hormonal and sex-specific drivers in meningiomas will be critical to devising effective and targeted therapeutic strategies.

Most atypical (WHO grade II) and malignant (WHO grade III) meningiomas harbor NF2 mutations and monosomy at chromosome 22q, for which there are no clear therapeutic options (9). Prognostic methylation signatures implicate epigenetic dysregulation in meningioma, yet actionable therapeutic targets remain elusive (10,11). The role of epigenetics in meningioma maintenance and progression is further highlighted by several reports of polycomb repressive complex (PRC) dysfunction, as well as global changes in methylation and recurrent mutations in epigenetic modifiers (12-17). Grade II meningioma are reported to harbor PRC complex upregulation and histone 3 lysine 27 trimethylation (H3K27me3) hypermethylation compared to grade I tumors (14). However, global DNA hypomethylation (13) and reduced H3K27me3 (15) are associated with increased risk of recurrence. These data strongly implicate epigenetic dysregulation in meningioma growth and malignancy, but highlight the need for a more nuanced stratification that extends the current histologic classification scheme. Furthermore, the functional implication and therapeutic utility of these alterations remains unknown.

Enhancer profiling using histone 3 lysine 27 acetyl chromatin immunoprecipitation sequencing (H3K27ac ChIP-seq) can identify clinically relevant stratifications and targetable dependencies that may not be apparent from genetic and transcriptional methods alone (18-22). Enhancer signaling informs key mediators of transcriptional control and gene expression programs. A subset of enhancers marked by particularly dense and long stretches of H3K27ac signal, designated as stretch enhancers or super enhancers (SEs), highlight genes important to cell identity that require robust expression (20,23,24). Thus, in addition to informing transcriptional networks and altered chromatin regulation, enhancer profiles highlight novel dependencies that are not apparent from RNA-sequencing or genomic approaches.

We selected a cohort enriched for aggressive tumors spanning all three histologic grades, as these represent the meningiomas with a critical need for new medical therapies. By integrating the enhancer landscape of 33 meningiomas with clinical and transcriptional data, we derived clinically relevant subgroups demonstrating robust predictive value for recurrence irrespective of histologic grading schemes. Transcriptional regulatory networks reveal distinct lineage and hormonal drivers that appear to maintain subgroup-specific enhancer networks. Despite the predominance of NF2 mutations in our cohort, tumor-specific epigenetic and transcriptional signaling enrich for pathways regulated by other recurrent genetic mutations, implicating epigenetic processes in driving oncogenic programs independent of genomic aberrations. Finally, we elucidated druggable, pan-meningioma and tumor-specific dependencies by targeting SE-associated signatures to provide a foundation for developing new therapeutic approaches to meningioma.

RESULTS

The enhancer landscape of meningioma

We analyzed the enhancer landscape by H3K27ac ChIP-seq in an aggressive and diverse cohort of 33 meningiomas (Fig. 1A). Whole exome sequencing (WES), RNA sequencing (RNA-seq) and DNA methylation analysis were performed for the majority of tumors (Supplementary Fig. S1). For a subset of samples, RNA-seq, WES and DNA methylation data were already available (17). Tumors spanned all histological grades and the cohort was evenly divided between male vs. female patients, recurrent vs. primary tumors and history of radiation vs. no adjuvant treatment. The median time to recurrence was 17 months and median overall survival was 35 months (Supplementary Table 1, Supplementary Data 1). To identify molecular features that stratify by prognosis and elucidate dependencies in the tumor subset with the greatest need for new therapeutic options, our cohort focused on an aggressive set of tumors. The majority of tumors harbored NF2 mutations and monosomy at chromosome 22. 55% of tumors displayed loss of 1p36, a known risk factor for recurrence (Supplementary Fig. S1). DNA methylation analysis confirmed co-clustering of all except two tumors of our cohort with an independent cohort of reference meningiomas (Fig. 1B) (25). Meningiomas are anatomically considered central nervous system (CNS) tumors based upon location and are thought to derive from arachnoid granulation (AG) cells in the meninges. To determine whether meningiomas transcriptionally resembled central nervous system (CNS) tumors or other cancers, we projected the meningioma samples onto a map generated from The Cancer Genome Atlas (TCGA) RNA-seq data, representative of over 30 different tumor types, revealing transcriptional similarities between meningioma and mesothelioma (which are also driven by NF2 mutations), sarcoma, testicular germ cell tumors and ovarian cancer (Fig. 1C). To investigate whether enhancers provide unique information about the relationship of meningiomas to normal cell-types and tissues, we utilized the H3K27ac Roadmap dataset from ENCODE (26,27) to generate normal sample clusters. Further, we obtained enhancer RNA (eRNA) data extracted from over 10,000 TCGA RNA-seq samples for cancer clustering (28). We then compared the enhancer profiles of meningiomas to the enhancers of normal cells and other cancer types (see Materials and Methods). Based on consensus clustering metrics, we identified 5 clusters in each dataset (Supplementary Fig. S2A). Each tumor or normal tissue type was composed of varying amounts of signal from each cluster. Brain tumors demonstrated high eRNA signal from one specific cluster, while another eRNA cluster was predominantly expressed in breast and prostate cancers, along with urothelial bladder carcinoma and diffuse large B-cell lymphoma (Fig. 1D). Relative to tumor models, meningiomas derived the most signal from the cluster of glioblastoma and low-grade glioma, and the cluster containing breast and prostate tumors (Fig. 1D). In comparison with normal cells and tissues, meningiomas were most similar to stem cells and to ovarian and breast tissues (Supplementary Fig. S2B). Epigenetically, meningiomas resembled both hormonally-driven cancers and primary malignant brain tumors, while the predominant transcriptional signal derived from other NF2-mutated tumors such as mesothelioma.

To broadly characterize the enhancer profile of meningiomas, we combined enhancers identified in individual tumors into a set of consensus meningioma enhancers. Enhancers

were assigned to their putative target genes by co-activation analysis of enhancer and gene expression within the boundaries of transactivation domains, as previously described (29). Top SE-associated genes comprised multiple regulators of MAPK signaling, including two dual-specificity phosphatase (DUSP) family members – DUSP1 and DUSP5 (Fig. 1E). Gene set enrichment analysis (GSEA) of SE-associated genes identified enrichment for Hippo, Wnt, Notch and Sonic hedgehog signaling pathways, as well as MAPK and Rho signaling, repression of cell death, and hormonal signaling pathways (Fig. 1F). Activation of these pathways may represent an epigenetic ‘second-hit’ in NF2-mutated meningiomas.

Top SEs were largely shared between different tumor grades and DUSP1 was a top SE-associated gene in all three grades (Supplementary Fig. S3A). SEs enriched in each grade were associated with higher H3K27ac signal and with increased expression of the predicted target gene within their respective grade compared to the rest of the cohort (Supplementary Fig. S3B). GO enrichment of genes associated with the top 100-enriched SEs in each grade revealed shared signaling pathways, such as hormone-responsive programs (progesterone response, ovulation cycle and mammary gland epithelial differentiation). Distinct pathways enriched in grade III tumors included neural programs and p38/MAPK signaling (Supplementary Fig. S3C).

To interrogate tumor-specific epigenetic and transcriptional pathways, we compared enhancer and transcriptional profiles of meningioma tissue to three normal AG cell models derived from post-mortem dissections of the superior sagittal sinus. 1447 SEs were unique to tumors, while 147 were lost in comparison to normal AG cultures (Supplementary Fig. S4A). One of the most downregulated SEs in tumor samples is predicted to regulate PLCH2 (Phospholipase C Eta 2; Supplementary Fig. S4A). PLCH2 resides on 1p36, a common site of copy number loss in meningiomas. The PLCH2 SE was specifically downregulated in comparison to neighboring SEs on the same cytoband, so may be a candidate tumor suppressor on 1p36. Gene set enrichment of top tumor-specific SE-associated genes revealed upregulation of pathways involved in epithelial-mesenchymal transition (EMT), Notch signaling, repression of cell differentiation and receptor tyrosine kinase signaling. AG SEs were enriched for programs involved in mucin glycosylation, cell polarity and vitamin metabolism (Supplementary Fig. S4B). Gene expression of predicted SE targets correlated with their enrichment in tumor vs. normal samples (Supplementary Fig. S4C). Transcriptional differences recapitulated a subset of altered pathways driven by meningioma-enriched SEs including GTPase, Notch, MAPK, Hippo and PIP signaling, although top differentially expressed genes were often distinct from the most differential SEs. Chromatin and lysine modification were specifically highlighted by RNA-seq and implicate global chromatin remodeling in meningioma pathology (Supplementary Fig. S4D). These data should be interpreted with the caveat that comparison of meningioma tissue to cultured cells may be influenced by culture-specific artifacts.

A direct comparison of motif enrichment, using normal AG cells as the background, identified progesterone receptor (PR) and glucocorticoid receptor as the most highly gained in meningiomas vs. normal enhancers, while AP-1, MED-2 and YY2 were lost in tumors (Supplementary Fig. S5A). The strong tumor PR motif enrichment combined with the epidemiological evidence implicating progesterone in meningioma pathogenesis, prompted

us to investigate whether PR plays a role in the tumor enhancer landscape. The PR signature was highly enriched for SE-associated genes, with nearly half of PR-regulated genes associated with SEs (hypergeometric p -value = $7.7e-25$) (Supplementary Fig. S5B and S5C). Pathways of Rho activity, phosphatidylinositol processing, and carbohydrate metabolism were also enriched, suggesting a broad role of PR-regulated programs in tumor signaling and metabolism (Supplementary Fig. S5D). To test whether progesterone stimulates growth in normal AG, AG cells were treated with progesterone, resulting in modest upregulation of cell proliferation, while treatment with the PR inhibitor, mifepristone, had opposing effects (Supplementary Fig. S5E).

We next compared irradiated vs. unirradiated and recurrence vs. primary tumors. Motif enrichment of differential enhancers (p -value <0.05 and \log_2 fold change >1) revealed that motifs targeted by the transcription factors ALX, LMX and ARID were enriched in primary tumors, while EGR, TFAP, SP and KLF family members were enriched in recurrent tumors (Supplementary Fig. S6A). KLF and SP and AP-1 motifs were enriched in irradiated samples, while GATA motifs were depleted (Supplementary Fig. S6B). We then analyzed pathways regulated by these differential enhancers. Recurrent tumors exhibit neuronal and glial signaling while primary tumors enrich for pathways involved in more mesodermal pathways (Supplementary Fig. S6C). Unirradiated tumors reflected similar signaling processes as primary tumors, potentially due to the moderate overlap of these two cohorts (Supplementary Fig. S6D). There were no significantly upregulated pathways in irradiated tumors. SEs associated with HOXB3 and SOX10 had greater signal in recurrent samples, while the known tumor suppressor MN1 was upregulated in unirradiated samples (Supplementary Fig. S6E and S6F).

Enhancers segregate tumors into prognostic and biologically distinct subgroups

To determine whether enhancers delineate clinically meaningful tumor subgroups, we performed non-negative matrix factorization (NMF) clustering on all 33 tumors using consensus meningioma enhancers. Clustering metrics revealed strong consensus at $k = 3$, with exclusion of one sample (Fig. 2A; Supplementary Fig. S7). These clusters stratified tumors into prognostic subgroups, with group 3 tumors exhibiting rapid recurrence (Fig. 2B). We integrated enhancer subgroup information with available clinical data and known predictors of recurrence, including 1p36 status, Heidelberg methylation cluster assignment, histological grade and history of radiation. While some of the above factors were individual predictors of recurrence free survival (RFS) (Supplementary Table 2), in a multivariable Cox proportional hazards model, only enhancer cluster and history of radiation were significantly predictive when combined into a multivariable analysis (Supplementary Table 3). Nearly all tumors were identified as meningiomas by the Heidelberg classifier, but only approximately 1/3 received a clear assignment into methylation subclasses. Tumors with the worst prognoses were more frequently unclassified, suggesting that expansion of the meningioma methylation classifier may be warranted, in particular with respect to rapidly recurrent tumors (Fig. 2C) (11). To determine whether methylation state informed prognosis independent of existing classifiers, we performed NMF clustering on our samples using the 10% most variable probes from the 450K methylation array. $K=5$ was selected due to the relatively higher cophenetic and silhouette scores (Supplementary Fig. S8A and S8B).

Consensus clustering assignment was used to segregate subgroups (Supplementary Fig. S9A). The methylation subgroups were plotted against enhancer classifications in a tanglegram, with lines connecting identical samples (Supplementary Fig. S9B). In our cohort, enhancer clustering provided a cleaner segregation and a prognostic advantage over methylation clustering (Supplementary Table 2), although one small subgroup of methylation clustering with 3 samples had a poorer prognosis.

Several individual SEs were also predictive of recurrence based upon their presence or absence in a sample (Supplementary Table 4). The strongest predictor of rapid recurrence was an SE associated with CDH5 (Cadherin 5; HR: 41.9, 95% CI: 4.6-378.5), a biomarker of metastatic breast cancer and high-grade glioma (30,31). A nearby SE at LRRC36 (Leucine Rich Repeat Containing 36) was the only positive prognostic predictor (HR: 0.1, 95% CI: 0.05-0.4; Supplementary Fig. S10). Clinical characteristics of enhancer subgroups revealed that group 3 tumors were enriched for, but not exclusive to, grade III tumors and male patients, while group 1 tumors had a greater proportion of grade II tumors, and group 2 tumors had a majority of grade I tumors. Both group 1 and group 2 patients had a greater proportion of female patients (Fig. 2D). History of radiation and primary vs. recurrent status of the tumor did not segregate between groups (Supplementary Fig. S11).

To validate our prognostic subgroups, we performed H3K27ac ChIP-seq on an additional 14 meningiomas (Supplementary Table 5). Tumors were subgrouped with single-sample gene set enrichment analysis (ssGSEA) using the top 100 differential enhancers from each subgroup from the discovery cohort as a signature. Unsupervised hierarchical clustering based on the scaled ssGSEA score, in combination with the maximal scaled subgroup score, was used to classify the validation cohort tumors. This method assigned the correct subgroup to the original cohort in 31/32 tumors. In every case, the subgroup assignment using the maximal ssGSEA scores was concordant between tumors on a given leaf (Fig. 2E) We then assessed whether this classification was prognostic in the validation cohort (Fig. 2F-I and Supplementary Table 6). Tumors in group 3 were more likely to recur irrespective of grade ($p=0.1$) (Fig. 2F and 2G). Within grade II, group 3 tumors were significantly more likely to recur ($p=0.0025$) (Fig. 2H and 2I).

We also confirmed that our subgroup classifier was relevant in a published independent cohort of tumors using gene expression data (17). We used the top 100 or 250 group 3 SE-associated genes to form a gene signature and stratified meningiomas by high vs. low expression, cut at the median (Supplementary Fig. S12A and S12B). Tumors with high expression of these signatures tended to have a higher recurrence rate (top 250 SEs: $p=0.138$; top 100 SEs: $p=0.161$).

To determine whether enhancer subgroups harbor distinct molecular drivers, we compared typical enhancer, SE and transcriptional profiles. While the top SEs were generally shared across subgroups (Fig. 3A), subgroup-enriched SEs highlighted specific programs and differential SEs within in each group (Fig. 3B; Supplementary Fig. S13A). Gene expression changes recapitulated a subset of SE signaling, although each data type presented additional unique pathway enrichments. Genes involved in cholesterol metabolism and repression of stem cell differentiation were notable within group 1. We therefore designated this group to

be ‘adipogenesis/cholesterol’. Mesodermal and muscle development pathways were upregulated in group 2, while neuronal programs were enriched in group 3 tumors (Fig. 3B and 3C). Two differentially expressed genes, CRYGN and SPOCK1, effectively stratified subgroups 1 and 2 vs. 3. CRYGN was upregulated in subgroups 1 and 2 vs. 3 (ANOVA p-value=0.00015, Student’s t-test: 1 vs. 3 p-value = 1.7e-4, 2 vs. 3 p-value = 7e-4) (Supplementary Fig. S13B and S13C). SPOCK1 marked subgroup 3 vs. 1 and 2 (ANOVA p-value=1.15e-5, Student’s t-test: 1 vs. 3 p-value = 2e-5, 2 vs. 3 p-value = 4.2e-4) (Supplementary Fig. S13D). Combinatorial expression of the PR network gene CRYGN vs. SPOCK1 effectively stratified the poorly prognostic subgroup 3 from subgroups 1 and 2 and may serve as a potential future clinically implementable assay to identify tumors with poor prognosis (Supplementary Fig. S13E).

There was a notable skewing of H3K27ac signal towards group 1 tumors, which was particularly evident in SEs (Supplementary Fig. S13A). Given the reported alterations in PRC complex members, we investigated whether gene expression changes or mutations could explain this bias. There was no enrichment of PRC complex mutations in the group, nor were there clear alterations of gene expression in these pathways. However, subgroup SEs enriched for targets of SUZ12, a member of the PRC complex (Supplementary Fig. S13F). Additionally, 3 out of 4 tumors with the highest number of SEs had mutations in the deacetylase SIRT2, predicted by 3 different algorithms to be deleterious (Supplementary Fig. S13G).

Enhancer networks reveal distinct transcriptional programs stratified by clinical characteristics and subgroups

As enhancers are associated with TF binding, we reasoned that enhancers with similar transcriptional drivers could be segregated into distinct modules based upon correlation of H3K27ac signal. Enhancer modules empower reconstruction of transcriptional circuitry by integrating TF expression data and enhancer motif enrichment for different modules. Degree of connectivity in both protein and transcriptional networks predicts critical genes in cell survival and disease prognosis (32-34). Thus, enhancer hubs within a given module may highlight enhancers and genes of particular importance. Module eigen-enhancers compared across clinical or biologic characteristics identify modules and predict transcriptional programs that are differentially enriched within a given trait. We therefore generated a weighted correlation network of enhancers from the meningioma enhancer peakset (Fig. 4A) (35,36). Enhancer networks exhibited clear scale-free topology and segregated cleanly into modules (Supplementary Fig. S14A and S14B). SEs were more highly connected than typical enhancers, both within and between modules (Supplementary Fig. S14C). SEs may therefore be of particular importance in maintaining the structure of epigenetic networks. Using the corresponding eigen-enhancer signal, we identified modules that were significantly altered between enhancer subgroup, sex, recurrence-free survival or Heidelberg methylation classification (Supplementary Fig. S14D). Enhancer subgroup and methylation classification were associated with the most differential module signal throughout the network relative to other features. There was a significant overlap between modules that were differential by enhancer subgroup and those that were distinct by methylation group,

highlighting the interplay between these epigenetic regulatory mechanisms in network structure (hypergeometric p-value = 0.005) (Supplementary Fig. S14E).

We next explored individual modules that were differentially enriched by tumor recurrence, 1p36 status or patient sex for further interrogation (Supplementary Fig. S14D). The subnetwork that was associated with rapid recurrence was highly enriched for regulators of neural crest differentiation and stem cell maintenance. HOXD family members and FOXM1, which were previously associated with malignant behavior (17), were also enriched in this module (Supplementary Fig. S15A). The 1p36-associated module was upregulated in tumors harboring 1p36 deletion. Motifs of two TFs on the 1p36 cytoband were highly enriched in this enhancer module. These TFs, HES5, a NOTCH-responsive repressive factor that regulates brain and cardiac development, and PAX7, which regulates myogenesis, may therefore be important transcriptional regulators associated with loss of 1p36 in meningioma (Supplementary Fig. S15B). Three sex-differential modules were enriched in female vs. male patients (Supplementary Fig. S15C). TFs predicted to regulate these modules were highly enriched for adipogenesis and circadian rhythm regulation. Furthermore, these TFs were upregulated in Genotype-Tissue Expression (GTEx) adipose and breast tissue and downregulated in GTEx brain tissue. These subnetworks revealed distinct transcriptional programs in male vs. female tumors.

To predict which TFs were driving subgroup differences, we generated subgroup-specific networks by selecting all modules that demonstrated subgroup-specific changes (ANOVA p-value <0.1) and assigning them to the subgroup with the highest eigen-enhancer enrichment (Fig. 4B; Supplementary Fig. S14D). Correlating TF expression with the module eigen-enhancer for each subgroup-specific module re-stratified enhancer subgroups despite being unsupervised, supporting a functional interaction between TF enrichments and enhancer subnetworks (Supplementary Fig. S16). We intersected this list with TF motifs enriched in each subgroup-specific module. The top ten TFs ranked by motif enrichment were used to build subgroup TF networks (Fig. 4C). Group 1 TFs were enriched for programs involved in cholesterol and adipogenesis as well as hormonal nuclear receptors (Fig. 4D). Group 2 TFs were enriched in mesodermal development, consistent with differential SE (Fig. 3B) and RNA-seq (Fig. 3C) programs (Fig. 4D). Group 3 TFs regulated neural crest development (Fig. 4D).

Given the over-representation of hormone receptor TFs in multiple subgroups and the reported intertumoral heterogeneity of PR, we investigated whether hormone receptor expression or activity distinguished meningioma subgroups. PR signature scores were significantly higher in the adipogenesis/cholesterol and mesodermal group (Fig. 4E). Conversely, AR signature was upregulated in the neural crest group (Fig. 4E). However, individual hormone receptors including androgen receptor (AR) (Supplementary Fig. S17A), estrogen receptor (ER) (Supplementary Fig. S17B), and PR (Supplementary Fig. S17C) demonstrated trends in expression, but did not differ consistently and significantly between groups. The difference between AR and PR expression separated subgroup 2 vs. 3 ($p < 0.05$) (Supplementary Fig. S17D). PR and the PR-regulated gene expression were positively and significantly correlated ($r = 0.64$, $p\text{-value} = 0.0013$) (Supplementary Fig. S17E). Hormone receptor activity, rather than expression alone, delineated subgroups. Thus, subgroup-

enriched TF networks implicate distinct transcriptional programs and highlight hormonal players in subgroup-specific tumor maintenance.

Meningioma SE-associated genes are druggable and tumor-specific dependencies

Given the lack of effective medical therapies for meningioma and our data demonstrating that SEs mark important genes for tumor cell survival, we sought to identify novel, druggable targets using SE-associated genes. First, we assessed the top consensus SEs to identify individual druggable genes. Among the top 10 SE-associated genes, only DUSP1 had an available inhibitor (Fig. 5A) (37). We also derived signatures from the top SE-associated genes in each subgroup and predict drugs to antagonize these signatures (see Materials and Methods) (Fig. 5A). We tested this panel of drugs against 6 meningioma cell lines and 2 normal AG cell lines to identify drugs with antitumor activity (Supplementary Table 7). Two existing meningioma models (CH157-MN and IOMM-Lee) were used along with 4 additional models derived in this study. Cells were maintained in DMEM with 7% fetal bovine serum (FBS). Of the 6 tumor cell lines tested, 3 were aggressive models to ensure drug efficacy in the tumors in greatest need of new therapeutics: DI-134, derived in-house from the poor prognosis/neural crest subgroup; CH157-MN, an existing grade III model; and IOMM-Lee, a model of unknown grade harboring genomic instability. Drug responses were benchmarked against the FAK inhibitor, GSK2256098, which is currently in clinical trials to target the NF2-mutated subset of meningiomas based on its efficacy *in vitro* in inhibiting growth of merlin-deficient mesothelioma (<https://clinicaltrials.gov/ct2/show/NCT02523014>).

Of the 17-drug panel, 7 drugs had an average maximum effect (E_{\max}) of > 50% reduction in cell viability vs. DMSO control (Fig. 5B). The DUSP1/6 inhibitor, BCI, had the strongest effect on cell viability with an $E_{\max} < 0.25$ in all 6 cell lines. Additional effective drugs included inhibitors of bromodomain (JQ1), MDM (RITA), aurora kinase (AT2983), FGFR (orantinib), heat shock proteins (KRIBB11), HIV protease (ritonavir) and Rho kinase (GSK269962A). FAK inhibition was minimally effective in any cell model with an average $E_{\max} > 0.5$ (Fig. 5C).

The SE assigned to DUSP1 was strong and present throughout the cohort, making it a rational target for pan-meningioma therapy (Supplementary Fig. S18A). We validated the screen results by treating 5 meningioma and a normal AG cultures with the same inhibitor (Fig. 6A). The BET inhibitor JQ1 reduced expression of DUSP1, confirming DUSP1 regulation by a SE (Fig. 6B). To confirm DUSP1 as a dependency in meningioma, we targeted DUSP1 by shRNA in the meningioma cell line, IOMM-Lee (Fig. 6C and 6D) and the newly derived meningioma model, DI-134 (Fig. 6E and 6F). Depletion of DUSP1 with two non-overlapping shRNAs reduced cell viability versus a non-targeting control (Fig. 6C-F). Knockout of DUSP1 via CRISPR-Cas9 in CH157-MN (Supplementary Fig. S18B and S18C) or IOMM-Lee (Supplementary Fig. S18D and S18E) impaired cell viability *in vitro*. Consistent with the reported phosphatase function of DUSP1, Treatment with BCI increased phosphorylation of ERK, JNK, and p38, and induced expression of cleaved caspase-3 and cleaved PARP, consistent with induction of apoptosis via known targets of DUSP1 (Fig. 6G). Depletion of DUSP1 in an orthotopic xenograft model using CH157-MN cells prolonged

mouse survival vs. non-targeting control (Fig. 6H-I). To test the efficacy of DUSP1/6 inhibition *in vivo* in the absence of restricted delivery, CH157-MN cells were implanted subcutaneously into flanks of immunodeficient mice. After one week of tumor growth, mice were treated twice daily with 10 mg/kg of BCI or an equivalent volume of DMSO via intraperitoneal injection. No toxicity was observed over the course of treatment (Supplementary Fig. S18F). Treatment with BCI decreased tumor weight ($p = 0.043$) (Fig. 6J) and tumor volume ($p = 0.029$) (Fig. 6K and 6L) compared to DMSO. Using enhancer profiling, we identified a set of novel drug candidates in meningioma and demonstrated the therapeutic potential of a DUSP1/6 inhibitor *in vivo*. DUSP1/6 inhibition is a promising therapeutic candidate that can be targeted for further compound development.

DISCUSSION

Although the majority of meningiomas are histologically benign, these tumors cause significant morbidity and mortality in many patients. Meningiomas that fail standard-of-care therapy of surgical resection and radiation lack effective medical therapies. Furthermore, clinicians face challenges selecting which patients should undergo radiotherapy after surgery, potentially exposing patients to unnecessary and permanent toxicity, based upon histologic grading alone. Methylation clustering provides additional prognostic stratification, but such studies do not provide actionable targets (11). Mutational profiling is one option for stratifying tumors, largely low grade ones (12,38). However, while mutations may serve as initiating events, the loss of a tumor suppressor, such as NF2, does not provide an actionable target, nor sufficiently account for oncogenic programs. We now propose an additional strategy to delineate meningiomas by risk of recurrence based upon novel prognostic subgroups of meningioma driven by distinct transcriptional drivers (Fig. 7). This stratification effectively discriminated high vs. low risk subgroups in a discovery and validation ChIP-seq cohort. A limitation of this study was the modest sample size, and thus future work will be necessary to further validate our findings regarding the prognostic potential of the identified subgroups. High-risk signatures applied to gene expression data trended towards significance for predicting rapid recurrence, suggesting that future work could investigate improved methods to extend the enhancer classification to apply to additional data types. Enhancer subgroups exhibit signatures of hormonal drivers and may be amenable hormonal therapies using progesterone antagonists. Across tumor grade and subgroup, SE signatures reveal novel druggable targets, which can inform future therapeutic development for tumors that have not responded to resection and radiation.

Meningiomas are anatomically classified as CNS tumors, but contextualizing them in the larger cancer landscape allows for improved molecular understanding and novel therapeutic strategies. Transcriptional and epigenetic data provide complementary, but unique insights into tumor biology. While transcriptional analyses reveal that meningiomas most closely resemble other NF2-mutated tumors, the enhancer profile of meningiomas demonstrates characteristics of both CNS malignancies and hormonally-driven tumors. Interrogation of the SE landscape implicates PR as a core transcriptional driver of a subset of tumors. These data provide a putative explanation for the strong epidemiological sex bias and case reports of meningiomas receding following discontinuation of progesterone agonists (3-7). The uneven responses reported in clinical trials may thus be driven by distinct epigenetic

subgroups of tumors. Further investigation into the specific biology of arachnoid cap cells that promote their responsiveness to progesterone is warranted.

Epigenetically dysregulated programs recapitulated pathways regulated by known meningioma driver mutations. Our cohort, which consisted largely of NF2-deficient tumors, demonstrated strong upregulation of not only Hippo, but also Notch, Wnt, and Sonic hedgehog signaling pathways. Dysregulation at the epigenetic level may reveal additional oncogenic drivers following NF2 loss in merlin-deficient tumors. SE pathways also highlight altered MAPK signaling and coordinated changes in the PIP pathway enzymes relative to normal AG cells.

By deriving enhancer networks, we identified epigenetic and transcriptional modules that correlate with a wide range of important clinical and genetic features of our cohort. Rapid recurrence was highly associated with neural crest progenitor and stem cell programs, as well as neuronal signaling pathways. The meninges are thought to derive from both mesenchymal and neural crest lineages, and thus, malignant tumors may reactivate developmental programs distinct from less aggressive, more mesenchymal tumors, with this distinction reflected in our reported enhancer-derived subgroups.

Finally, targeted therapies for meningiomas are lacking. There is a critical lack of drug options for patients with aggressive tumors for whom resection and radiation are insufficient. We demonstrate the utility of enhancer profiling to identify potent drug candidates for meningioma treatment. SE signatures effectively elucidate meningioma dependencies and predict drugs that potently and selectively kill meningioma cells *in vitro* and *in vivo*, paving the way for further investigation into novel therapeutic options in treatment of meningioma.

METHODS

Derivation of meningioma tissue and models

Meningioma samples were acquired from excess surgical resection tissues from patients at the Cleveland Clinic. All specimens were reviewed by a neuropathologist upon resection prior to banking and again prior to sample processing. Appropriate written informed consent was obtained from patients in accordance with a Cleveland Clinic Institutional Review Board (IRB)-approved protocol (090401) and the study was performed in accordance with the Declaration of Helsinki. Clinical data were collected under IRB 16956 from Cleveland Clinic. All studies involving human patients were conducted in accordance with the Declaration of Helsinki. Clinical information was not available for de-identified (DI) samples. Tissue was snap-frozen and stored at -80°C . For cell models, tissues were dissociated using the Papain dissociation system (Worthington Biomedical Corp; LK003150) and cultured in DMEM supplemented with 1% penicillin/streptomycin and 7% fetal bovine serum (FBS). Short tandem repeat analyses were performed to authenticate the identity of each tumor model used in this article annually. Cells were stored at -160°C when not being actively cultured. All cells were thawed within 1 month of these experimental procedures. All experiments conformed to the relevant regulatory standards.

CH157-MN was provided by the Gillespie lab at the University of Alabama-Birmingham and IOMM-Lee was provided by the Jensen lab at the University of Utah.

Arachnoid cell derivation

Arachnoid cells were derived from postmortem tissue via the body donation program at the Cleveland Clinic. Arachnoid granulations from the superior sagittal sinus were dissected and dissociated using the Papain dissociation system (Worthington Biomedical Corp; LK003150) and cultured in DMEM with 1% penicillin/streptomycin and 10% fetal bovine serum (FBS). Cells were immortalized at passage 6 by transfection with SV40-Large T antigen (addgene plasmid #21826).

Quantitative RT-PCR

Trizol reagent (Sigma-Aldrich) was used to isolate total cellular RNA from cell pellets. The qScript cDNA Synthesis Kit (Quanta BioSciences) was used for reverse transcription into cDNA. Quantitative real-time PCR was performed by using Applied Biosystems 7900HT cyclor using SYBR-Green PCR Master Mix (Thermo Fisher Scientific). Quantitative PCR (qPCR) primers used in this study were human DUSP1-fwd: 5'-ACCACCACCGTGTTCAACTTC-3', DUSP1-rev: 5'-TGGGAGAGGTCGTAATGGGG-3', beta-2 microglobulin-fwd: 5'-GAGGCTATCCAGCGTACTCCA-3' and beta-2 microglobulin-rev: 5'-CGGCAGGCATACTCATCTTTT-3', GAPDH-fwd: 5'-TGACAACCTTGGTATCGTGGAAGG-3', GAPDH-rev: 5'-AGGCAGGGATGATGTTCTGGAGAG-3'

Western blotting

Cells were collected and lysed in RIPA buffer (50 mM Tris-HCl, pH 7.5; 150 mM NaCl; 0.5% NP-40; 50 mM NaF with protease inhibitors) and incubated on ice for 30 minutes. Lysates were centrifuged at 4°C for 15 minutes at 14,000 rpm, and supernatant was collected. The Pierce BCA protein assay kit (Thermo Scientific, cat #23225) was utilized to determine of protein concentration. Equal amounts of protein samples were mixed with SDS Laemmli loading buffer, boiled for 10 minutes, and electrophoresed using NuPAGE Bis-Tris Gels, then transferred onto PVDF membranes. TBS-T supplemented with 5% non-fat dry milk was used for blocking for a period of 1 hour followed by blotting with primary antibodies at 4°C for 16 hours. Blots were washed 3 times for 5 minutes each with TBS-T and then incubated with appropriate secondary antibodies in 5% non-fat milk in TBS-T for 1 hour. For all western immunoblot experiments, blots were imaged using BioRad Image Lab software and subsequently processed using Adobe Illustrator to create the figures. The following antibodies were used for Western blot: p44/42 MAPK (Erk1/2), 1:1000 (CST, cat #4695, 137F5), phospho-p44/42 MAPK (Erk1/2) (Thr202/Tyr204), 1:1000 (CST, cat #4370, D13.14.4E), p38 MAPK 1:1000 (Proteintech, 14064-1-AP), phospho-p38 (Thr180/Tyr182), 1:2000 (CST, cat #4511, D3F9), SAPK/JNK, 1:1000, (CST, cat #9252), phospho-SAPK/JNK (Thr183/Tyr185), 1:1000 (CST, cat #4668T, 81E11), cleaved caspase-3 (Asp175), 1:1000 (CST, cat #9664S, 5A1E), HRP-conjugated GAPDH, 1:40,000 (Proteintech, cat #HRP-60004) and DUSP1, 1:1000 (LifeSpan BioSciences, cat #LS-C332288).

In vitro drug studies

For *in vitro* cell viability assays, 1000 cells/well were plated in a 96-well plate in DMEM with 7% FBS on day 0, then treated 24 hours later with the corresponding drug or DMSO at an equivalent percent volume to the highest drug concentration. Progesterone (Sigma cat #P8783-5G, CAS #57-83-0) was resuspended in 100% ethanol. Mifepristone/RU486 (Fisher scientific, cat. #501011574, CAS #84371-65-3) was resuspended in DMSO. Cell viability was assayed 48 hours later using cellTiter-Glo reagent (Promega; G7572). Plates were shaken at room temperature for 15 min and then read for luminescence output.

For the compound drug screen assay, compounds and DMSO vehicle controls were transferred in a volume of 10 nL to black, clear-bottom 1,536-well plates (Greiner; 789092) using an acoustic transfer system (ATS) Gen4+ instrument (EDC Biosystems). Cells were dispensed in a volume of 10 μ L, and a density of 500 cells per well by using a Multidrop Combi liquid handler (Thermo Fisher Scientific; 5840300). Plates were incubated at 37°C and 5% CO₂ for 72 h, at which point CellTiter-Glo reagent (Promega; G7572) was added to each well using the Multidrop Combi instrument. Plates were shaken at room temperature for 15 min and then read for luminescence output by using an EnVision plate reader (Perkin Elmer). Maximum effect was then calculated as the greatest reduction in cell viability versus the average of the DMSO controls for the corresponding plate for each cell line. The following drugs were tested: GNE-0877 (cat #S7367, CAS #1374828-69-9, SelleckChem), orantinib (TSU-68, SU6668) (cat #S1470, CAS #252916-29-3, SelleckChem), (+)-JQ1 (cat #S7110, CAS #1268524-70-4, SelleckChem), SB525334 (cat #S1476, CAS #356559-20-1, SelleckChem), ritonavir (cat #S1185, CAS #155213-67-5, SelleckChem), ropivacaine Hcl (cat #S4058, CAS #132112-35-7, SelleckChem), (+)-bicuculline (cat #S7071, CAS #485-49-4, SelleckChem), fenofibrate (cat #S1794, CAS #49562-28-9, SelleckChem), gatifloxacin (cat #S1340, CAS #112811-59-3, SelleckChem), piperacillin Sodium (cat #S4222, CAS #59703-84-3, SelleckChem), dual specificity protein phosphatase 1/6 Inhibitor, BCI (cat #317496, CAS #15982-84-0, MilliporeSigma), RITA (cat #S2781, CAS #213261-59-7, SelleckChem), KRIBB11 (cat #S8402, CAS #342639-96-7, SelleckChem), AT9283 (cat #S1134, CAS #896466-04-9, SelleckChem), GSK2699 (cat #S7687, CAS #850664-21-0 (free base), SelleckChem), reboxetine mesylate (cat #S3199, CAS #98769-84-7, SelleckChem) and GSK2256098 (cat #S8523, CAS #1224887-10-8, SelleckChem).

In vitro cell viability assays

Lentiviral constructs expressing non-overlapping shRNAs directed against DUSP1 (TRCN0000355637, TRCN0000367631) or a non-targeting control shRNA (TRCN0000231489) with no targets in the human genome were obtained from Sigma-Aldrich. DUSP1-targeting shRNAs were assayed for knockdown efficiency by qPCR and were then used for all following experiments. For CRISPR-Cas9 experiments, sgRNAs were cloned into the lentiCRISPR v2 plasmid (Addgene #52961). DUSP1 sgRNA: 5'-CGTCCAGCAACACCACGGCG-3'. 293T cells were used to generate lentiviral particles by co-transfecting the packaging vectors psPAX2 and pMD2.G using a standard calcium phosphate transfection method in DMEM media containing 1% penicillin/streptomycin. For cell viability assays, meningioma models were transduced with the corresponding

lentiviral constructs and selected 48 hours later using 1 µg/mL of puromycin. Cells were selected for 72 hours, then plated at a density of 1000 cells/well in a 96-well format with 12 wells per condition. Cell viability was assayed by incubating with cellTiter-Glo while shaking for 20 minutes and then read for luminescence.

In vivo studies

In vivo drug studies were performed by implanting 1 million cells into the flank of NSG (NOD.Cg-Prkdcscid Il2rgtm1Wjl/SzJ; The Jackson Laboratory) mice. Once tumors had formed mice were randomly assigned into drug vs. treatment group by a blinded investigator. Mice were treated with BCI (cat #317496, CAS #15982-84-0, MilliporeSigma) or an equivalent percentage of DMSO resuspended in 0.9% saline by intraperitoneal injection daily. All murine experiments were performed under an animal protocol approved by the University of California, San Diego, Institutional Animal Care and Use Committee. Healthy, wild-type male mice of NSG background, 4–6 wk old, were randomly selected and used in this study for flank injection. For intracranial xenograft studies, mice were orthotopically implanted with 10,000 cells and were sacrificed upon observation of neurological signs by a blinded investigator. None of the mice had experienced any treatment or procedures before the experiments described. Mice were housed together in a controlled environment with 14 h of light and 10 h of dark per day. Animal husbandry staff at the University of California, San Diego, regularly observed all animals, and no more than five mice were housed in each cage. Animals were monitored until tumor size exceeded 2.0 cm in the longest dimension.

RNA-seq library preparation

RNA-seq was performed as previously described (22). Total RNA was extracted from flash frozen, pulverized tissue using the miRNeasy mini kit (Qiagen, cat #217004) in accordance with the manufacturer protocols. Libraries were prepared and sequenced by Genewiz. Stranded RNA library preparation was performed with ribosomal RNA depletion according to instructions from the manufacturer (Epicentre). Paired-end sequencing was performed on the Illumina HiSeq 2500 with 2 × 150 bp paired-end read configuration.

Whole exome sequencing

Whole exome sequencing (WES) was performed as previously described (21). DNA from flash-frozen tumor samples was extracted using the Quick-DNA 96 Plus kit (Zymo). The Agilent SureSelect Human All Exon 50-Mb target enrichment kit v4 was used to capture all human exons for deep sequencing using the vendor's protocol v2.0.1. The SureSelect Human All Exon Kit targets regions of 50 Mb in total size, which is approximately 1.7% of the human genome. In brief, 3 µg genomic DNA was sheared with a Covaris S2 to a mean size of 150 bp. Five hundred nanograms of library DNA was hybridized for 24 h at 65 °C with the SureSelect baits. 15 ng final exome-enriched library (without barcode) was used as a template in a 50-µl PCR reaction. The Herculase II Fusion enzyme (Agilent) was used together with the NEBNext Universal PCR primer for Illumina and NEBNext Index primer (NEB #E7335S) under the following conditions: the initial denaturation step for 2 min at 98 °C was followed by four cycles of 30s at 98 °C, 30s at 57 °C, 1 min. at 72 °C, and a final

step of 10 min. at 72 °C. Barcoded samples were then sequenced on the HiSeq2000 in 2 × 100-bp paired-end mode.

H3K27ac chromatin immunoprecipitation and sequencing

Chromatin immunoprecipitation (ChIP) was performed as previously described (22). Briefly, 5–10 mg of flash-frozen primary meningioma tumors was pulverized, crosslinked using 1.5% formaldehyde and sonicated to fragment sizes of 200-800 bp. Samples were incubated overnight with 5 µg H3K27ac antibody per ChIP experiment (Active Motif; 39133). Enriched DNA was quantified by using PicoGreen (Invitrogen) and ChIP libraries were amplified and barcoded by using the ThruPLEX DNA-seq library preparation kit (Rubicon Genomics) according to the manufacturer's recommendations. Following library amplification, DNA fragments were agarose gel (1.0%) size selected (<1 kb), analyzed using a Bioanalyzer (Agilent Technologies) and sequenced at Genewiz by using Illumina HiSeq 2500 2x150-bp paired-end reads.

RNA-seq data analysis

For the subset of samples for which previously published RNA-seq data were available, data were downloaded from GEO (GSE101638). To match the data format of this series, only single-end reads were used and were trimmed to 75 bp using BBDuk from the BBMap toolset. Trim Galore was used to trim adaptors and remove low quality reads (39). Reads were quantified against Gencode v29 using Salmon with correction for fragment-level GC bias, positional bias and sequence-specific biases (40). Transcripts were summarized to gene level and processed to transcripts per million (TPM) using the R/Bioconductor (<http://www.R-project.org/>) package DESeq2 (41) and batch-corrected using ComBat from the R *sva* package (42). Comparisons were performed using contrasts in DESeq2 followed by Benjamini-Hochberg adjustment to correct for false discovery rate. For gene set enrichment analysis (GSEA) comparing tumor vs. normal, a pre-ranked list was generated and weight by the inverse of the FDR multiplied by the sign of the log₂ fold change. This list was used as input to the desktop GSEA software (43). Gene sets tested were GO biological processes, Reactome and KEGG. Enrichment maps for all gene sets significant at an FDR<0.2 with an edge cutoff (gene set similarity) of 0.375 were visualized using the Bader Lab Enrichment Map plugin (44) in Cytoscape v3.6 (45).

Whole exome analysis

For the subset of samples for which previously published whole exome sequencing data were available, data were downloaded from GEO (GSE101638). Low quality reads and adaptors were trimmed using Trim Galore (39). BWA-MEM version 0.7.17 was used to align paired-end exome sequencing reads to the hg19 reference genome (46). SAMtools (47) was used to sort and index BAMs. PCR duplicates were removed with PicardTools (<http://broadinstitute.github.io/picard/>). Single-nucleotide variants and indels were identified with the Genome Analysis Toolkit v3.8 (48) in accordance with the Genome Analysis Toolkit best practices with the principal steps of base quality score recalibration, variant genotyping for singlenucleotide variants and indels and variant hard-filtering with standard recommendations (49,50). Variants with predicted deleterious effects were annotated using ANNOVAR (51). SNVs or indels predicted to be deleterious by 2/3 of PolyPhen2, whole-

exome SIFT or MutationTaster with a frequency of <1% in the 1000 Genomes Project, NHLBI-ESP and CompleteGenomes were annotated as mutations.

Methylation and copy number variation analysis

Genomic DNA was extracted as described for whole exome sequencing and samples were sent for Infinium MethylationEPIC BeadChip Kit (Illumina). Probes from the Infinium MethylationEPIC BeadChip were downsampled to only those intersecting with the 450K chip. These probes were processed with the R packages minfi (52) and CopywriteR (53), which were used to identify CNVs for NF2 and the corresponding regions of chromosome 22 and for 1p36.

Meningioma classification by methylation

Methylation data was uploaded to the Heidelberg meningioma classification tool (25) at: <https://www.molecularneuropathology.org/mnp>. Meningioma methylation group was assigned to the classification with the highest clustering score. Meningiomas not matching any classification (score <0.3), were considered unclassified.

Methylation clustering

Normalized methylation data for CNS tumors was downloaded from GSE109379 and meningioma cohort data were processed using the same pipeline as described (25). Data from GSE109379 were clustered with the UMAP algorithm using the R package uwot (<https://github.com/jlmeville/uwot>) using the parameters: n_neighbors=100, learning_rate=0.5, init="random", pca=50, min_dist=0.4. New samples were embedded onto the map.

H3K27ac ChIP-seq data processing and peak calling

H3K27ac ChIP-seq was processed following the ENCODE guidelines. FASTQ reads were trimmed to remove low quality reads and adaptors with Trim Galore (39) and uniquely mapped reads were aligned to the human reference genome hg19/GRCh37 with the Burrows-Wheeler Aligner to generate BAMs (46). BAMs were sorted and indexed with SAMtools (47). PCR duplicates were removed using PicardTools (<http://broadinstitute.github.io/picard/>). Peaks were called using the MACS2 (54) callpeak function on the ChIP-seq BAM file using the following parameters: BAMPE for paired-end reads, scaling to the larger dataset, the default log2 fold change enrichment of 2 vs. input and a p-value cutoff of 1e-5. Consensus peaksets and normalized H3K27ac densities were generating using the R/Bioconductor package DiffBind (<https://bioconductor.org/packages/release/bioc/vignettes/DiffBind/inst/doc/DiffBind.pdf>) using the following parameters: score=score=DBA_SCORE_TMM_MINUS_FULL, bUseSummarizeOverlaps = T. Peaks were required to be present in at least 2/33 tumor samples or 1/3 normal samples. Overlapping peaks were merged. Peaks intersecting ENCODE blacklisted regions v1 (55), on haplotype chromosomes or on chromosomes X or Y were excluded from analysis. Peaks within 2.5 kb of a known transcription start site were also excluded. Bigwig tracks were generated using the DeepTools (v3.1.2) (56) bamCoverage command with RPKM normalization. Genomic coverage heatmaps were generated using the DeepTools (56) computeMatrix followed by plotHeatmap functions. Peaks were visualized using Integrative

Genomics Viewer software (57). Super enhancers were called using ROSE (24) and default parameters. Gene set enrichment plots for tumor SEs were generated using ClueGO (58) for GO BP, KEGG and Reactome gene sets and visualized in Cytoscape (45). Tumor-specific and normal-specific SEs were called by intersecting consensus tumor SEs with consensus normal SEs. Waterfall plots of log₂ fold change were derived using the normalized values from DiffBind. Tumor vs. normal SE enrichments were generated by inputting the genes associated with SEs with a log₂ fold change >0.5 into ClueGO (58).

Gene-enhancer pairs

Gene-enhancer pairs were called using the R/Bioconductor (<http://www.R-project.org/>) package InTad (29). Genes with a significant ($p < 0.1$), positively-correlated enhancer were assigned to the enhancer within the transactivation domain that had the most significant correlation. Enhancers with no significantly correlated genes were assigned to the nearest expressed gene.

Tumor vs. normal motif enrichment

BAM files for tumor or normal H3k27ac ChIP-seq or the corresponding input samples were merged using sambamba (59) and centered around nucleosome-free regions using the Homer (60) findpeaks function with the 'histone' and 'nfr' flags to center peaks around the nucleosome free regions. Enriched motifs in tumor peaks were identified using findMotifsGenome with the normal peaks as background and vice versa to identify normal-enriched motifs.

NMF clustering

Non-negative matrix factorization was performed using the R (<http://www.R-project.org/>) package NMF (61) on normalized enhancer and SE peak densities. Ranks from 2 to 10 were analyzed with 'nrun=100'. For enhancers, one sample was excluded from the final clustering due to a silhouette width <0.5. For NMF clustering of methylation data, the top 10% most variable probes were used.

Progesterone receptor network analysis

The progesterone receptor (PR) network was derived by identifying genes highly correlated with PR ($r > 0.4$). A genome-wide list of peaks containing a PR motif was derived using HOMER (60) scanMotifGenomeWide function with default settings. This list was intersected with the enhancer peakset and genes that were correlated with PR and had a PR motif in their assigned enhancer. This final gene list was used to infer the PR-regulated gene network. This gene list was intersected with the identified super enhancer list to generate the overrepresentation analysis for PR-regulated genes and SE-associated genes. The gene set enrichment plot for PR-regulated genes was generated using ClueGO for GO BP, KEGG and Reactome gene sets and visualized in Cytoscape.

Drug predictions

Drug predictions were performed using the genes associated with the top 100 super enhancers with the greatest mean H3K27ac signal density for each subgroup. This list was

input to the LINCS Clue database (62) using the “Query” tool. The top 10 compound perturbations that were inversely correlated with the gene signature were selected for each subgroup. The most negatively correlated drug representing that category was selected to represent the compound in the drug panel.

UMAP RNA-seq

TCGA pan-cancer data was downloaded from freeze 1.3 of the TCGA PanCan Atlas at the Synapse website (<https://www.synapse.org/#!Synapse:syn4557014>). Data were logged and plotted using the R (<http://www.R-project.org/>) package uwot (<https://github.com/jlmeville/uwot>) with the following parameters: n_neighbors=100, learning_rate = 0.5, init = “random”, pca=50, min_dist = 0.4, ret_model=T. ComBat batch-corrected, log2-transformed meningioma RNA-seq were projected onto this map.

H3K27ac processing for ENCODE Roadmap clustering

Roadmap H3K27ac ChIP-seq bigwig files were downloaded from <https://www.encodeproject.org/matrix/?type=Experiment&award.project=Roadmap&searchTerm=H3K27ac&assembly=hg19>. FASTQ files from this study were trimmed to 36 bp using BBDuk from BBMap (<https://sourceforge.net/projects/bbmap/>) to match the Encode Roadmap data and were processed as described in the ENCODE workflow (<https://github.com/ENCODE-DCC/chip-seq-pipeline2>). ENCODE blacklisted regions (55) were subtracted and bigwigs were merged across all 213 samples using DeepTools (56) multiBigwigSummary with a bin size of 10,000. The top 10% of most variable enhancers were input into consensusClusterPlus (63) (maxK=25, reps=50). Optimal cluster size was determined by the greatest change in area under the cumulative density function curve at $K>3$.

Enhancer RNA data processing

Enhancer RNA (eRNA) data processed from TCGA pan-cancer RNA-seq data (28) were kindly provided by Chen et al. (28) Single-end FASTQ files were trimmed with Trim Galore (39) and aligned using the workflow provided by NCI Genomic DNA Commons, (https://docs.gdc.cancer.gov/Data/Bioinformatics_Pipelines/Expression_mRNA_Pipeline/). The STAR (64) 2-pass tool was used to generate BAM files. Gene expression values were derived using HT-Seq (65) count and summarized to gene level according to Gencode v22 annotation. The data were imported into R using DiffBind (<https://bioconductor.org/packages/release/bioc/vignettes/DiffBind/inst/doc/DiffBind.pdf>) and signal was called restricted to a bed file of the ~10,000 enhancers used in the original report (28). Data were normalized using log2 RPKM to match the original report. The datasets were merged, quantile normalized across sample and then mean-centered across each eRNA. The optimal cluster size was determined using the R/Bioconductor (<http://www.R-project.org/>) package ConsensusClusterPlus (63) (maxK=25, reps=50). Optimal cluster size was determined by the greatest change in area under the cumulative density function curve at $K>3$.

Roadmap and eRNA grade of membership model

Grade of membership models were derived using the R/Bioconductor (<http://www.R-project.org/>) package CountClust (66) at the default tolerance of 0.1. Cluster membership for each sample was averaged across tissue type and the resulting tissue cluster scores were mean-centered for each cluster across tissue type. Z-scores were plotted in a heatmap.

Signature scores

PR signature scores were derived using single sample GSEA (ssGSEA) from GenePattern (67) using the derived PR signature. AR signature scores were derived using ssGSEA using the PID_AR_PATHWAY from C2-curated gene sets from the Molecular Signatures Database (MsigDB) (43).

Enhancer networks – WGCNA

Enhancer networks were derived using the normalized values for the tumor consensus enhancer peakset and the R (<http://www.R-project.org/>) package WGCNA (36). The pickSoftThreshold function was used to select the lowest soft thresholding power β that demonstrated a scale-free topology model fitted with an $R^2 > 0.9$. An adjacency matrix accounting for only positive correlations was generated with $\beta = 8$. The dynamicTreeCut method was used with a minimum cluster size of 40 and height of 0.998 to create a dendrogram and modules from the dissimilarity matrix, generating 53 modules. The moduleEigengenes function was used to calculate the eigen-enhancer for each module. The eigen-enhancers were used in clinical correlation analyses with relevant statistics described in figure legends.

Ternary plots

Ternary plots for group- or grade-enriched SEs were derived by summing the log₂ fold change for each SE to 1 and creating a ratio by dividing the log₂ fold change for each subgroup or grade over the summed log₂ fold change. These ratios were then squared and plotted with each subgroup ratio indicating one dimension along the ternary axes. Gene set enrichment plots for tumor SEs were generated using ClueGO²⁷ for GO BP, KEGG and Reactome gene sets.

TF module enrichment

Transcription factor (TF) networks were derived using the Regulatory Genomics Toolbox (RGT) (68). All tumor BAMs were merged using sambamba (59) merge and the RGT HINT tool was used to identify TF footprints in the merge tumor BAM across the tumor enhancer peakset. Motif enrichment was calculated for all tumor enhancers and for the enhancers of each individual module using the motifanalysis matching tool. Motifs from HOCOMOCO (69), Homer (60) and JASPAR (70) were used. Motif enrichment for each module vs. the background of all tumor enhancers was then calculated using Fisher's exact test. To account for multiple testing across many enhancers, p-values were adjusted using the Benjamini-Hochberg method. If multiple motifs for the same TF were identified, the lowest motif enrichment FDR was used.

Module and subgroup TF networks

For each module, enriched motifs were filtered using RNA-seq data to include expressed TFs that were correlated with the module eigen-enhancer $r > 0.1$. To determine TF networks for a subgroup, TFs filtered by the above criteria were ranked by motif enrichment within each subgroup-enriched module. TF ranks were then summed across subgroup-enriched modules and the top 10 TFs with the lowest rank value (i.e. most enriched) that were present in at least 50% of the subgroup-enriched modules were selected for visualization. TF networks were visualized using Cytoscape (45). Gene set enrichment analysis for TFs in a module or subgroup was performed using Enrichr (71).

Supplementary Material

Refer to Web version on PubMed Central for supplementary material.

ACKNOWLEDGMENTS

We appreciate critical input and feedback from the members of the Rich laboratory. This work was supported by grants provided by NIH: CA217066 (B.C.P.); CA217065 (R.C.G.); CA197718, CA154130, CA169117, CA171652, NS087913, NS089272, NS103434, CA238662 (J.N.R.), CPRIT award, ALSF young investigator award, Rally research grant, BEAR Necessities Pediatric Cancer Foundation Grant, Children's Cancer Research Fund award, and Baylor College of Medicine Junior Faculty Award (S.C.M). We also thank the Gillespie lab at the University of Alabama-Birmingham and the Jensen lab at the University of Utah for providing CH157-MN and IOMM-Lee cells, respectively. We appreciate the assistance of Mary McGraw and Dr. Christopher Hubert in obtaining samples. We thank the patients and donors who provided the tissue used in this study and acknowledge Dr. Richard Drake and Dr. Jennifer McBride from the Cleveland Clinic for their assistance in deriving arachnoid granulation models.

Financial support: This work was supported by grants provided by NIH: CA217066 (B.C.P.); CA217065 (R.C.G.); CA197718, CA238662, NS103434 (J.N.R.), CPRIT award, ALSF young investigator award, Rally research grant, BEAR Necessities Pediatric Cancer Foundation Grant, Children's Cancer Research Fund award, and Baylor College of Medicine Junior Faculty Award (S.C.M).

REFERENCES

- Ostrom QT, Gittleman H, Truitt G, Boscia A, Kruchko C, Barnholtz-Sloan JS. CBTRUS Statistical Report: Primary Brain and Other Central Nervous System Tumors Diagnosed in the United States in 2011-2015. *Neuro-Oncol.* 2018;20:iv1–86. [PubMed: 30445539]
- Suppiah S, Nassiri F, Bi WL, Dunn IF, Hanemann CO, Horbinski CM, et al. Molecular and translational advances in meningiomas. *Neuro-Oncol.* 2019;21:i4–17. [PubMed: 30649490]
- Custer B, Longstreth W, Phillips LE, Koepsell TD, Van Belle G. Hormonal exposures and the risk of intracranial meningioma in women: a population-based case-control study. *BMC Cancer.* 2006;6:152. [PubMed: 16759391]
- Patterson A, Elashaal A. Fast-Growing Meningioma in a Woman Undergoing Fertility Treatments. *Case Rep Neurol Med.* 2016;2016:1–3.
- Farina P, Lombardi G, Touat M, Sanson M. Successful treatment of multiple intracranial meningiomas with mifepristone (RU486). *J Clin Oncol.* 2014;32:TPS2108–TPS2108.
- Grunberg SM, Weiss MH, Spitz IM, Ahmadi J, Sadun A, Russell CA, et al. Treatment of unresectable meningiomas with the antiprogestone agent mifepristone. *J Neurosurg.* 1991;74:861–6. [PubMed: 2033444]
- Grunberg SM, Weiss MH, Russell CA, Spitz IM, Ahmadi J, Sadun A, et al. Long-term administration of mifepristone (RU486): clinical tolerance during extended treatment of meningioma. *Cancer Invest.* 2006;24:727–33. [PubMed: 17162554]
- Ji Y, Rankin C, Grunberg S, Sherrod AE, Ahmadi J, Townsend JJ, et al. Double-Blind Phase III Randomized Trial of the Antiprogestin Agent Mifepristone in the Treatment of Unresectable Meningioma: SWOG S9005. *J Clin Oncol.* 2015;33:4093–8. [PubMed: 26527781]

9. Bi WL, Greenwald NF, Abedalthagafi M, Wala J, Gibson WJ, Agarwalla PK, et al. Genomic landscape of high-grade meningiomas. *Npj Genomic Med.* 2017;2:15.
10. Nassiri F, Mamatjan Y, Suppiah S, Badhiwala JH, Mansouri S, Karimi S, et al. DNA methylation profiling to predict recurrence risk in meningioma: development and validation of a nomogram to optimize clinical management. *Neuro-Oncol.* 2019;21:901–10. [PubMed: 31158293]
11. Sahn F, Schrimpf D, Stichel D, Jones DTW, Hielscher T, Schefzyk S, et al. DNA methylation-based classification and grading system for meningioma: a multicentre, retrospective analysis. *Lancet Oncol.* 2017;18:682–94. [PubMed: 28314689]
12. Brastianos PK, Horowitz PM, Santagata S, Jones RT, McKenna A, Getz G, et al. Genomic sequencing of meningiomas identifies oncogenic SMO and AKT1 mutations. *Nat Genet.* 2013;45:285–9. [PubMed: 23334667]
13. Gao F, Shi L, Russin J, Zeng L, Chang X, He S, et al. DNA Methylation in the Malignant Transformation of Meningiomas. Rao J, editor. *PLoS ONE.* 2013;8:e54114. [PubMed: 23349797]
14. Harmancı AS, Youngblood MW, Clark VE, Co kun S, Henegariu O, Duran D, et al. Integrated genomic analyses of de novo pathways underlying atypical meningiomas. *Nat Commun.* 2017;8:14433. [PubMed: 28195122]
15. Katz LM, Hielscher T, Liechty B, Silverman J, Zagzag D, Sen R, et al. Loss of histone H3K27me3 identifies a subset of meningiomas with increased risk of recurrence. *Acta Neuropathol (Berl).* 2018;135:955–63. [PubMed: 29627952]
16. Paramasivam N, Hübschmann D, Toprak UH, Ishaque N, Neidert M, Schrimpf D, et al. Mutational patterns and regulatory networks in epigenetic subgroups of meningioma. *Acta Neuropathol (Berl).* 2019;138:295–308. [PubMed: 31069492]
17. Vasudevan HN, Braunstein SE, Phillips JJ, Pekmezci M, Tomlin BA, Wu A, et al. Comprehensive Molecular Profiling Identifies FOXM1 as a Key Transcription Factor for Meningioma Proliferation. *Cell Rep.* 2018;22:3672–83. [PubMed: 29590631]
18. Cejas P, Drier Y, Dreijerink KMA, Brosens LAA, Deshpande V, Epstein CB, et al. Enhancer signatures stratify and predict outcomes of non-functional pancreatic neuroendocrine tumors. *Nat Med.* 2019;25:1260–5. [PubMed: 31263286]
19. Gimple RC, Kidwell RL, Kim LJY, Sun T, Gromovsky AD, Wu Q, et al. Glioma Stem Cell Specific Super Enhancer Promotes Polyunsaturated Fatty Acid Synthesis to Support EGFR Signaling. *Cancer Discov.* 2019;9:1248–67. [PubMed: 31201181]
20. Lin CY, Erkek S, Tong Y, Yin L, Federation AJ, Zpatka M, et al. Active medulloblastoma enhancers reveal subgroup-specific cellular origins. *Nature.* 2016;530:57. [PubMed: 26814967]
21. Mack SC, Pajtler KW, Chavez L, Okonechnikov K, Bertrand KC, Wang X, et al. Therapeutic targeting of ependymoma as informed by oncogenic enhancer profiling. *Nature.* 2018;553:101–5. [PubMed: 29258295]
22. Mack SC, Singh I, Wang X, Hirsch R, Wu Q, Villagomez R, et al. Chromatin landscapes reveal developmentally encoded transcriptional states that define human glioblastoma. *J Exp Med.* 2019;216:1071–90. [PubMed: 30948495]
23. Hnisz D, Abraham BJ, Lee TI, Lau A, Saint-André V, Sigova AA, et al. Super-Enhancers in the Control of Cell Identity and Disease. *Cell.* 2013;155:934–47. [PubMed: 24119843]
24. Whyte WA, Orlando DA, Hnisz D, Abraham BJ, Lin CY, Kagey MH, et al. Master Transcription Factors and Mediator Establish Super-Enhancers at Key Cell Identity Genes. *Cell.* 2013;153:307–19. [PubMed: 23582322]
25. Capper D, Jones DTW, Sill M, Hovestadt V, Schrimpf D, Sturm D, et al. DNA methylation-based classification of central nervous system tumours. *Nature.* 2018;555:469–74. [PubMed: 29539639]
26. Davis CA, Hitz BC, Sloan CA, Chan ET, Davidson JM, Gabdank I, et al. The Encyclopedia of DNA elements (ENCODE): data portal update. *Nucleic Acids Res.* 2018;46:D794–801. [PubMed: 29126249]
27. ENCODE Project Consortium. An integrated encyclopedia of DNA elements in the human genome. *Nature.* 2012;489:57–74. [PubMed: 22955616]
28. Chen H, Li C, Peng X, Zhou Z, Weinstein JN, Liang H, et al. A Pan-Cancer Analysis of Enhancer Expression in Nearly 9000 Patient Samples. *Cell.* 2018;173:386–399.e12. [PubMed: 29625054]

29. Okonechnikov K, Erkek S, Korbel JO, Pfister SM, Chavez L. InTAD: chromosome conformation guided analysis of enhancer target genes. *BMC Bioinformatics*. 2019;20:60. [PubMed: 30704404]
30. Fry SA, Robertson CE, Swann R, Dwek MV. Cadherin-5: a biomarker for metastatic breast cancer with optimum efficacy in oestrogen receptor-positive breast cancers with vascular invasion. *Br J Cancer*. 2016;114:1019–26. [PubMed: 27010749]
31. Mao X -g., Xue X -y., Wang L, Zhang X, Yan M, Tu Y -y., et al. CDH5 is specifically activated in glioblastoma stemlike cells and contributes to vasculogenic mimicry induced by hypoxia. *Neuro-Oncol*. 2013;15:865–79. [PubMed: 23645533]
32. Han J-DJ, Bertin N, Hao T, Goldberg DS, Berriz GF, Zhang LV, et al. Evidence for dynamically organized modularity in the yeast protein–protein interaction network. *Nature*. 2004;430:88–93. [PubMed: 15190252]
33. Horvath S, Zhang B, Carlson M, Lu KV, Zhu S, Felciano RM, et al. Analysis of oncogenic signaling networks in glioblastoma identifies ASPM as a molecular target. *Proc Natl Acad Sci*. 2006;103:17402–7. [PubMed: 17090670]
34. Jeong YJ, Oh HK, Park SH, Bong JG. Association between inflammation and cancer stem cell phenotype in breast cancer. *Oncol Lett*. 2018;15:2380–6. [PubMed: 29434947]
35. Langfelder P, Horvath S. WGCNA: an R package for weighted correlation network analysis. *BMC Bioinformatics*. 2008;9:559. [PubMed: 19114008]
36. Zhang B, Horvath S. A general framework for weighted gene co-expression network analysis. *Stat Appl Genet Mol Biol*. 2005;4:Article17.
37. Molina G, Vogt A, Bakan A, Dai W, Queiroz de Oliveira P, Znosko W, et al. Zebrafish chemical screening reveals an inhibitor of Dusp6 that expands cardiac cell lineages. *Nat Chem Biol*. 2009;5:680–7. [PubMed: 19578332]
38. Clark VE, Harmancı AS, Bai H, Youngblood MW, Lee TI, Baranoski JF, et al. Recurrent somatic mutations in POLR2A define a distinct subset of meningiomas. *Nat Genet*. 2016;48:1253–9. [PubMed: 27548314]
39. Martin M Cutadapt removes adapter sequences from high-throughput sequencing reads. *EMBnet.journal*. 2011;17:10.
40. Patro R, Duggal G, Love MI, Irizarry RA, Kingsford C. Salmon provides fast and bias-aware quantification of transcript expression. *Nat Methods*. 2017;14:417–9. [PubMed: 28263959]
41. Love MI, Huber W, Anders S. Moderated estimation of fold change and dispersion for RNA-seq data with DESeq2. *Genome Biol*. 2014;15:550. [PubMed: 25516281]
42. Leek JT, Johnson WE, Parker HS, Jaffe AE, Storey JD. The sva package for removing batch effects and other unwanted variation in high-throughput experiments. *Bioinforma Oxf Engl*. 2012;28:882–3.
43. Subramanian A, Tamayo P, Mootha VK, Mukherjee S, Ebert BL, Gillette MA, et al. Gene set enrichment analysis: A knowledge-based approach for interpreting genome-wide expression profiles. *Proc Natl Acad Sci*. 2005;102:15545–50. [PubMed: 16199517]
44. Merico D, Isserlin R, Stueker O, Emili A, Bader GD. Enrichment Map: A Network-Based Method for Gene-Set Enrichment Visualization and Interpretation. Ravasi T, editor. *PLoS ONE*. 2010;5:e13984. [PubMed: 21085593]
45. Shannon P, Markiel A, Ozier O, Baliga NS, Wang JT, Ramage D, et al. Cytoscape: a software environment for integrated models of biomolecular interaction networks. *Genome Res*. 2003;13:2498–504. [PubMed: 14597658]
46. Li H, Durbin R. Fast and accurate long-read alignment with Burrows-Wheeler transform. *Bioinforma Oxf Engl*. 2010;26:589–95.
47. Li H, Handsaker B, Wysoker A, Fennell T, Ruan J, Homer N, et al. The Sequence Alignment/Map format and SAMtools. *Bioinforma Oxf Engl*. 2009;25:2078–9.
48. McKenna A, Hanna M, Banks E, Sivachenko A, Cibulskis K, Kernysky A, et al. The Genome Analysis Toolkit: a MapReduce framework for analyzing next-generation DNA sequencing data. *Genome Res*. 2010;20:1297–303. [PubMed: 20644199]
49. DePristo MA, Banks E, Poplin R, Garimella KV, Maguire JR, Hartl C, et al. A framework for variation discovery and genotyping using next-generation DNA sequencing data. *Nat Genet*. 2011;43:491–8. [PubMed: 21478889]

50. Van der Auwera GA, Carneiro MO, Hartl C, Poplin R, Del Angel G, Levy-Moonshine A, et al. From FastQ data to high confidence variant calls: the Genome Analysis Toolkit best practices pipeline. *Curr Protoc Bioinforma*. 2013;43:11.10.1-33.
51. Yang H, Wang K. Genomic variant annotation and prioritization with ANNOVAR and wANNOVAR. *Nat Protoc*. 2015;10:1556–66. [PubMed: 26379229]
52. Aryee MJ, Jaffe AE, Corrada-Bravo H, Ladd-Acosta C, Feinberg AP, Hansen KD, et al. Minfi: a flexible and comprehensive Bioconductor package for the analysis of Infinium DNA methylation microarrays. *Bioinformatics*. 2014;30:1363–9. [PubMed: 24478339]
53. Kuilman T, Velds A, Kemper K, Ranzani M, Bombardelli L, Hoogstraat M, et al. CopywriteR: DNA copy number detection from off-target sequence data. *Genome Biol*. 2015;16:49. [PubMed: 25887352]
54. Zhang Y, Liu T, Meyer CA, Eeckhoute J, Johnson DS, Bernstein BE, et al. Model-based analysis of ChIP-Seq (MACS). *Genome Biol*. 2008;9:R137. [PubMed: 18798982]
55. Amemiya HM, Kundaje A, Boyle AP. The ENCODE Blacklist: Identification of Problematic Regions of the Genome. *Sci Rep*. 2019;9:9354. [PubMed: 31249361]
56. Ramírez F, Ryan DP, Grüning B, Bhardwaj V, Kilpert F, Richter AS, et al. deepTools2: a next generation web server for deep-sequencing data analysis. *Nucleic Acids Res*. 2016;44:W160–5. [PubMed: 27079975]
57. Robinson JT, Thorvaldsdóttir H, Winckler W, Guttman M, Lander ES, Getz G, et al. Integrative genomics viewer. *Nat Biotechnol*. 2011;29:24–6. [PubMed: 21221095]
58. Bindea G, Mlecnik B, Hackl H, Charoentong P, Tosolini M, Kirilovsky A, et al. ClueGO: a Cytoscape plug-in to decipher functionally grouped gene ontology and pathway annotation networks. *Bioinforma Oxf Engl*. 2009;25:1091–3.
59. Tarasov A, Vilella AJ, Cuppen E, Nijman IJ, Prins P. Sambamba: fast processing of NGS alignment formats. *Bioinformatics*. 2015;31:2032–4. [PubMed: 25697820]
60. Heinz S, Benner C, Spann N, Bertolino E, Lin YC, Laslo P, et al. Simple combinations of lineage-determining transcription factors prime cis-regulatory elements required for macrophage and B cell identities. *Mol Cell*. 2010;38:576–89. [PubMed: 20513432]
61. Gaujoux R, Seoighe C. A flexible R package for nonnegative matrix factorization. *BMC Bioinformatics*. 2010;11:367. [PubMed: 20598126]
62. Duan Q, Flynn C, Niepel M, Hafner M, Muhlich JL, Fernandez NF, et al. LINCS Canvas Browser: interactive web app to query, browse and interrogate LINCS L1000 gene expression signatures. *Nucleic Acids Res*. 2014;42:W449–460. [PubMed: 24906883]
63. Wilkerson MD, Hayes DN. ConsensusClusterPlus: a class discovery tool with confidence assessments and item tracking. *Bioinforma Oxf Engl*. 2010;26:1572–3.
64. Dobin A, Davis CA, Schlesinger F, Drenkow J, Zaleski C, Jha S, et al. STAR: ultrafast universal RNA-seq aligner. *Bioinforma Oxf Engl*. 2013;29:15–21.
65. Anders S, Pyl PT, Huber W. HTSeq—a Python framework to work with high-throughput sequencing data. *Bioinforma Oxf Engl*. 2015;31:166–9.
66. Dey KK, Hsiao CJ, Stephens M. Visualizing the structure of RNA-seq expression data using grade of membership models. *PLoS Genet*. 2017;13:e1006599. [PubMed: 28333934]
67. Reich M, Liefeld T, Gould J, Lerner J, Tamayo P, Mesirov JP. GenePattern 2.0. *Nat Genet*. 2006;38:500–1. [PubMed: 16642009]
68. Gusmao EG, Dieterich C, Zenke M, Costa IG. Detection of active transcription factor binding sites with the combination of DNase hypersensitivity and histone modifications. *Bioinforma Oxf Engl*. 2014;30:3143–51.
69. Kulakovskiy IV, Vorontsov IE, Yevshin IS, Sharipov RN, Fedorova AD, Rumynskiy EI, et al. HOCOMOCO: towards a complete collection of transcription factor binding models for human and mouse via large-scale ChIP-Seq analysis. *Nucleic Acids Res*. 2018;46:D252–9. [PubMed: 29140464]
70. Khan A, Fornes O, Stigliani A, Gheorghe M, Castro-Mondragon JA, van der Lee R, et al. JASPAR 2018: update of the open-access database of transcription factor binding profiles and its web framework. *Nucleic Acids Res*. 2018;46:D260–6. [PubMed: 29140473]

71. Chen EY, Tan CM, Kou Y, Duan Q, Wang Z, Meirelles GV, et al. Enrichr: interactive and collaborative HTML5 gene list enrichment analysis tool. *BMC Bioinformatics*. 2013;14:128. [PubMed: 23586463]

Author Manuscript

Author Manuscript

Author Manuscript

Author Manuscript

SIGNIFICANCE

Enhancer landscapes inform prognostic classification of aggressive meningiomas, identifying tumors at high risk of recurrence, and reveal previously unknown therapeutic targets. Druggable dependencies discovered through epigenetic profiling potentially guide treatment of intractable meningiomas.

Author Manuscript

Author Manuscript

Author Manuscript

Author Manuscript

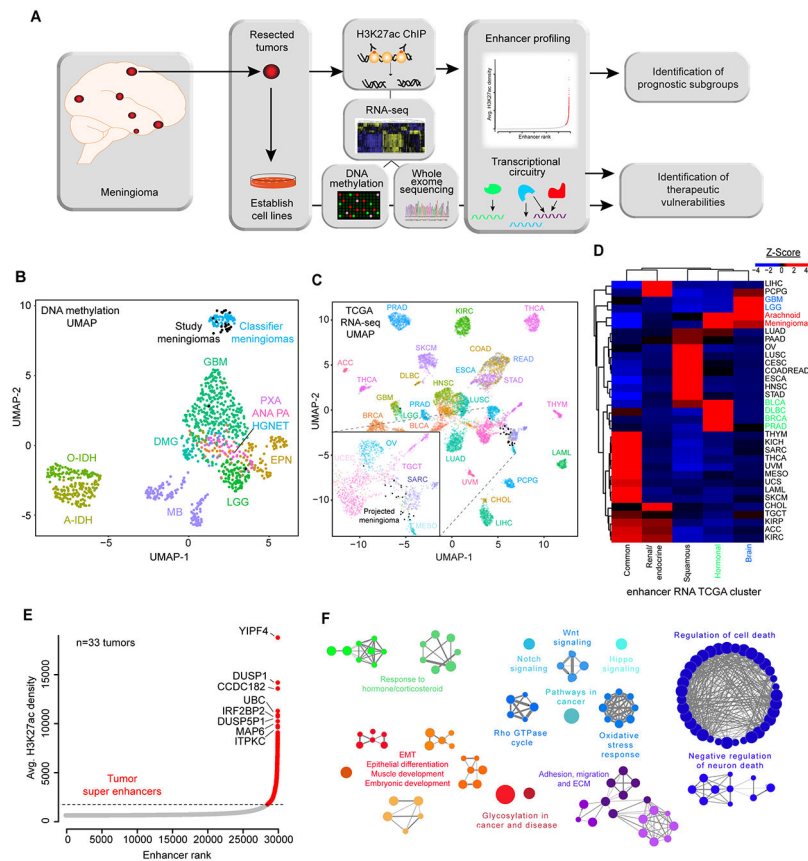


Figure 1. The enhancer and super enhancer landscape of meningiomas. (A) Overview of study design and goals. (B) UMAP projection of meningioma methylation state onto Heidelberg central nervous system (CNS) tumor dataset. Meningiomas from this study, in black, projected onto Heidelberg “classifier meningiomas”, in blue. (C) UMAP projection of meningioma RNA-seq onto TCGA RNA-seq data. Inset: Meningiomas (black) clustered with mesothelioma (MESO - green), sarcoma (SARC - purple) and testicular germ cell tumors (TGCT – pink), and near ovarian (OV – aqua) and uterine corpus endometrial carcinoma (UCEC – light pink). (D) Unsupervised hierarchical clustering of Z-scores for enhancer cluster signal generated from the grade-of-membership model for TCGA enhancer RNA (eRNA) from 10,000 samples and over 30 tumor types was clustered into 5 groups, which were used to generate a grade of membership model. Tumor types were then clustered based upon the amount of signal from each group. Meningiomas have the most signal from brain tumors (blue) and from hormonally-driven tumors (green) (BRCA: breast cancer, PRAD: prostate cancer). (E) Plot of consensus tumor enhancers. Super enhancers (SEs) are indicated in red above the inflection point of the graph. (F) ClueGO analysis of SE-associated genes. Enrichments are shown for Reactome, GO BP and KEGG pathways with a false discovery rate <0.05. Bubble size is proportional to number of genes overlapping the pathway.

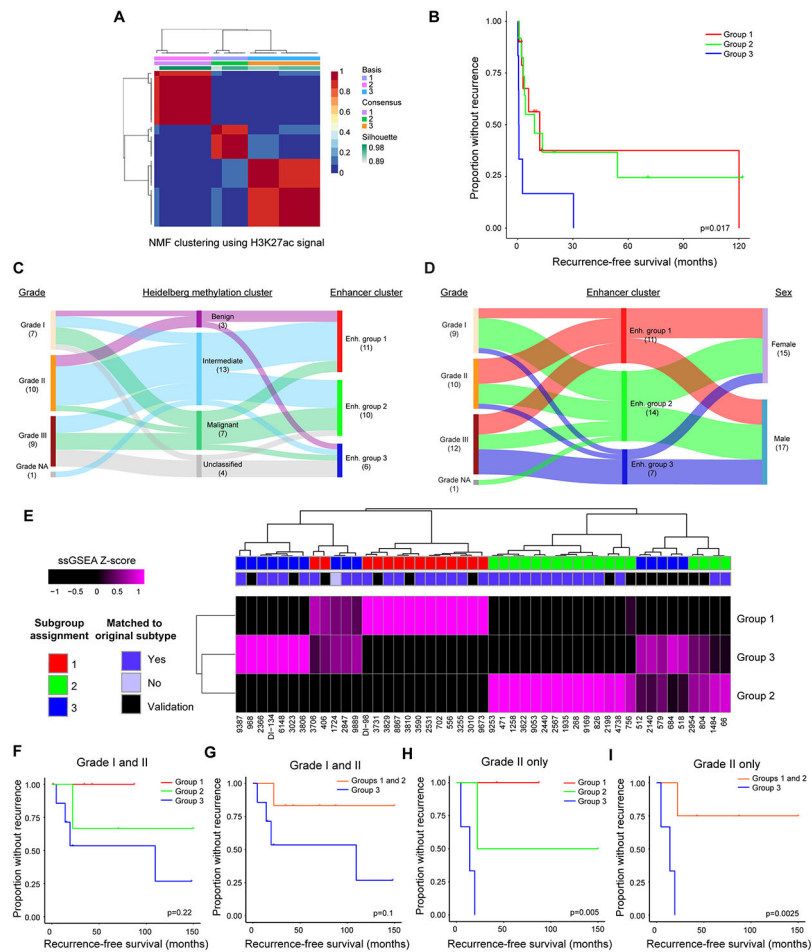


Figure 2. Enhancers delineate biologically distinct meningioma subgroups.

(A) Non-negative matrix factorization clustering of meningioma enhancer signal reveals 3 distinct subgroups. (B) Kaplan-Meier curves of recurrence-free survival stratified by enhancer subgroup. Logrank test was used to perform paired comparisons. Group 1 vs. 3: $p < 0.001$; group 2 vs. 3: $p < 0.001$; group 1 vs. 2: NS. (C) Sankey plot indicating the relationship of Heidelberg methylation cluster with grade and enhancer subgroup. Only the 27 samples with available methylation data were included in the plot. (D) Sankey plot indicating the relationship of enhancer subgroup with grade and sex. (E) Unsupervised hierarchical clustering of tumors based upon scaled ssGSEA score for the top 100 differential enhancers per subgroup. Tumors from the original and validation sets were scored and clustered together and subgroups were assigned based on the maximal ssGSEA score. (F) Kaplan-Meier curve for the validation cohort segregated by enhancer subgroup. (G) Kaplan-Meier curve for the validation cohort comparing groups 1 and 2 vs. 3. (H) Kaplan-Meier curve for grade II tumors in the validation cohort segregated by enhancer subgroup. (I) Kaplan-Meier curve for grade II tumors in the validation cohort comparing groups 1 and 2 vs. 3. ssGSEA: single-sample gene set enrichment analysis. p-values were generated using a logrank test.

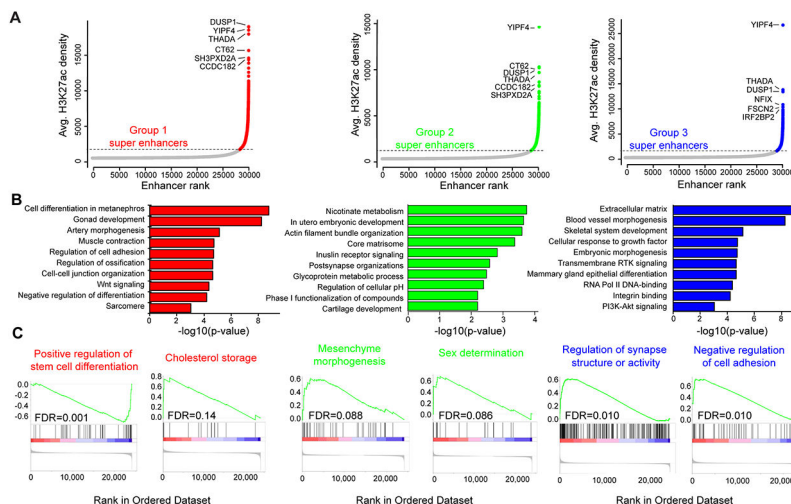


Figure 3. Enhancer subgroups are biologically distinct.

(A) Plot of consensus super enhancers (SEs) for each subgroup. Colored points represent SEs defined as signal above the inflection point of the curve. Gene labels are the predicted SE-associated genes. (B) ClueGO gene set enrichment analysis for subgroup-enriched SE-associated genes. Enrichment for GO BP, KEGG or Reactome pathways of the top 100 enriched SE-associated genes for each subgroup. (C) Gene set enrichment analysis of differentially expressed genes between tumor and normal for Reactome, KEGG and GO BP pathways. Genes were pre-ranked by the inverse of the false discovery rate multiplied by the sign of the fold change.

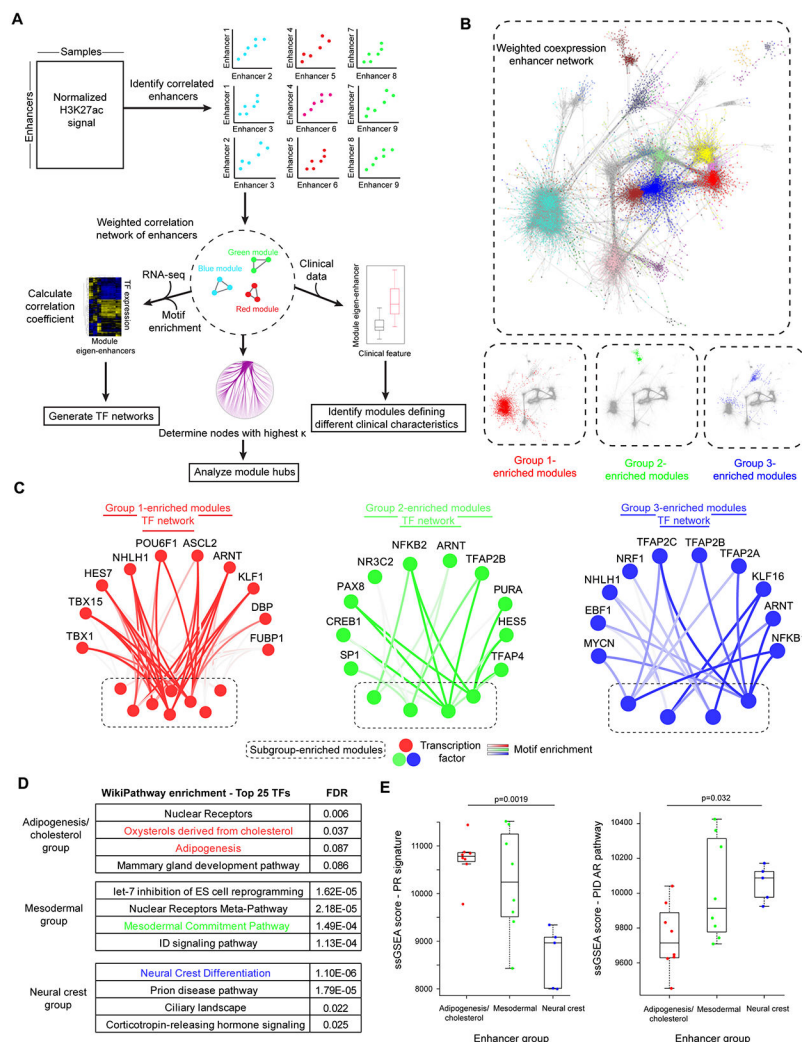


Figure 4. Enhancer networks reveal distinct transcriptional programs across subgroups. (A) Overview of method for generating enhancer correlation network and subsequent downstream analyses. (B) Visualization of the weighted enhancer network, with nodes colored based on module membership. Highlighted below are modules that are significantly different between subgroups, colored based upon the subgroup in which the eigen-enhancer is most enriched. (C) Transcriptional networks predicted to regulate subgroup-enriched modules for each subgroup. The top ten transcription factors (TFs) correlated with the most subgroup-specific networks at a correlation coefficient >0.4 were included in the network. Edges are colored by TF-module correlation, with higher intensity indicating correlation. Subgroup-specific modules are at the bottom of each network and are colored by module name. (D) Enrichment analysis of top 25 TFs in subgroup-specific modules. (E) Boxplot of single sample gene set enrichment analysis (ssGSEA) score for progesterone receptor regulatory network signature (left) or androgen receptor signature (right) stratified by enhancer subgroup. ssGSEA scores were derived from RNA-seq data from the 21 subgrouped samples for which these data were available. Comparisons were performed by

one-way ANOVA followed by Tukey's HSD. Boxplots are represented as the median plus interquartile range.

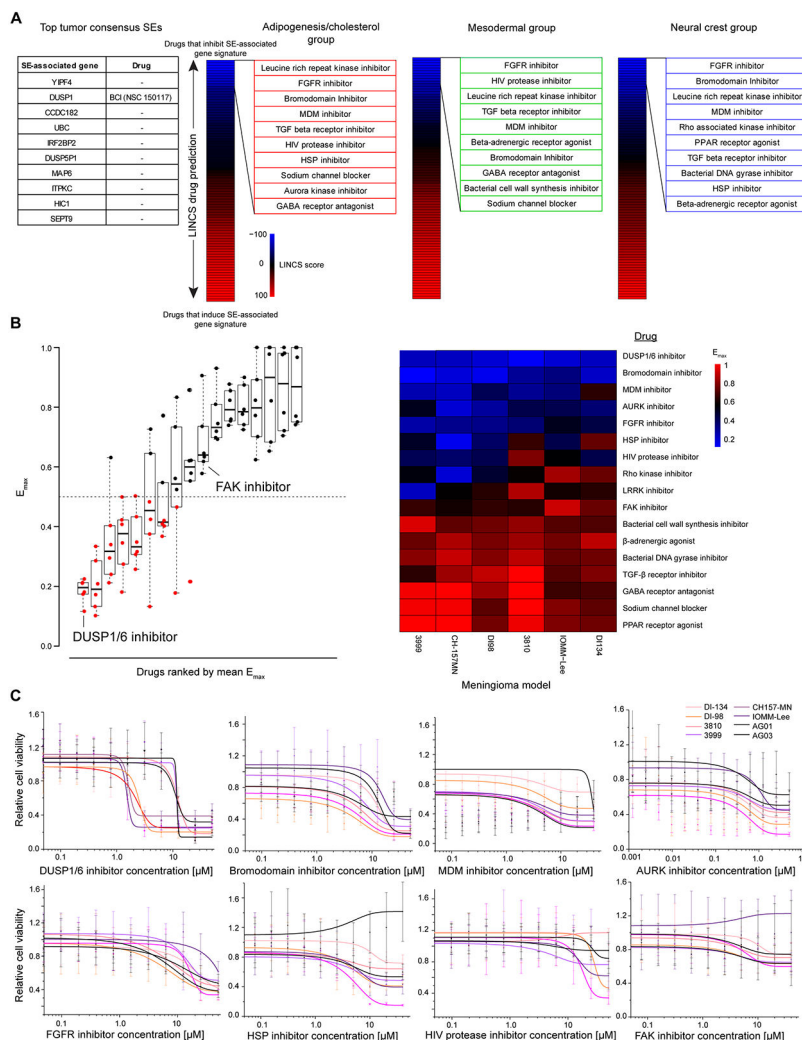


Figure 5. SE-associated genes are critical, druggable targets in vitro.

(A) Selection of drugs based upon SE profiles. Targetable SEs among individual top meningioma super enhancers (SEs) were limited to DUSP1 (left). Signatures were derived using the top 100 subgroup consensus SEs. These gene lists were used as input for the LINCS database which predicts drugs inversely and positively correlated with a gene set. Drugs were ranked from negatively to positively correlated based upon LINCS score. The top 10 compound classes inversely correlated with the SE gene signature from each subgroup were used to derive the drug panel. (B) Results of the screening 17 compounds across 6 meningioma and two arachnoid granulation (AG) models. Maximum drug efficacy (E_{max}) values are plotted as a boxplot (left), ranked from lowest to highest average E_{max} . E_{max} was calculated by comparing all tested drug concentrations to DMSO control and selecting the lowest value. E_{max} values plotted on a heatmap (right) were ranked from lowest (top, blue) to highest (bottom, red) E_{max} . Boxplots are represented as the median plus interquartile range. (C) Dose-response curves for each of the 7 compounds with an average $E_{max} < 0.5$ and the FAK inhibitor. Meningioma models are plotted in shades of red. Normal AG models are in black. Data are represented as mean \pm SD. Sigmoidal curves were fit using a dose-response function.

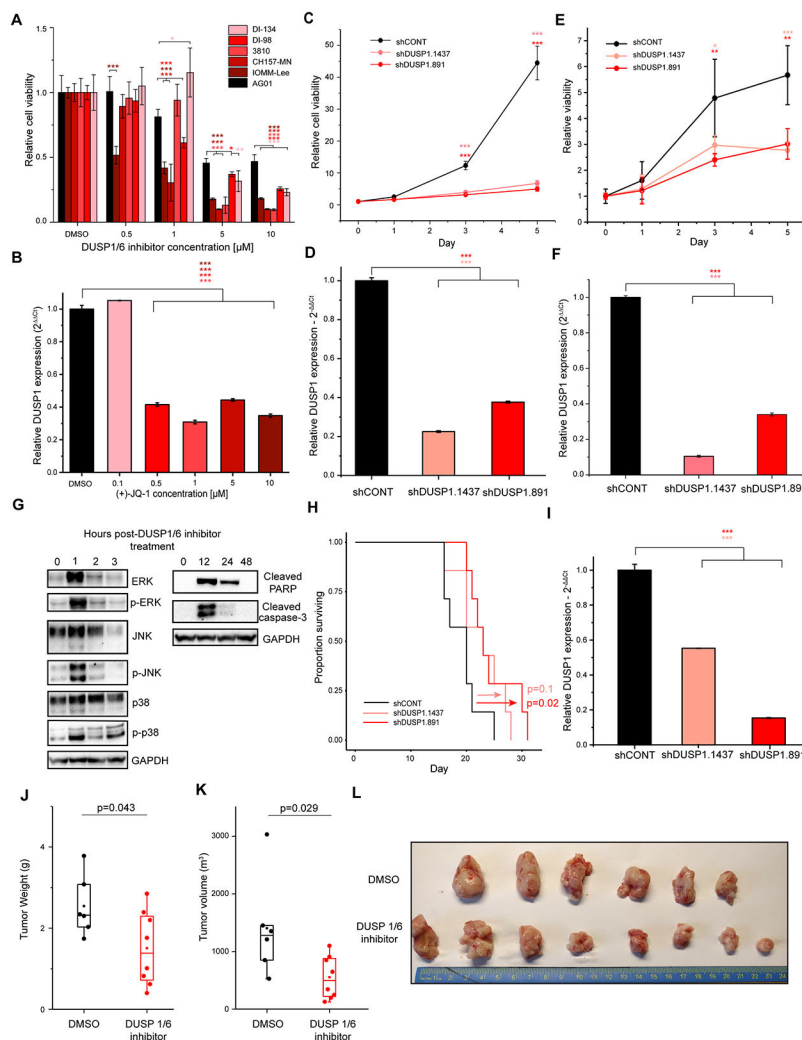


Figure 6. DUSP1 is a meningioma dependency *in vitro* and *in vivo*.

(A) Cell viability of meningioma models treated with BCI. Cell viability was calculated for each model relative to DMSO control (black). p-values were calculated using one-way ANOVA. Data are represented as mean \pm SD. (B) Downregulation of DUSP1 following treatment with the BET bromodomain inhibitor (+)-JQ-1. Cells were treated for 24 hours with a range of concentrations and then assayed for DUSP1 expression by qPCR. Data are represented as mean \pm SD. (C) Time course of cell viability following knockdown of DUSP1 in IOMM-Lee cells vs. non-targeting control. Conditions were compared using student's t-test. Data are represented as mean \pm SD. (D) Depletion of DUSP1 following transduction of one of two DUSP1-targeting shRNAs versus non-targeting control in IOMM-Lee cells. Data are represented as mean \pm SD. (E) Time course of cell viability following knockdown of DUSP1 in DI-134 cells vs. non-targeting control. Conditions were compared using student's t-test. Data are represented as mean \pm SD. (F) Depletion of DUSP1 following transduction of one of two DUSP1-targeting shRNAs versus non-targeting control in DI-134 cells. Data are represented as mean \pm SD. (G) Western blot to assay targets of DUSP1 and markers of apoptosis following treatment with 5 μ M of DUSP1/6

inhibitor. **(H)** Survival following intracranial xenograft of the meningioma model CH157-MN immunodeficient mice. Meningioma cells were transduced with non-targeting control shRNA (black line) or one of two independent shRNAs targeting DUSP1 (red lines). p-values were calculated using a logrank test. **(I)** DUSP1 expression in CH157-MN cells after transduction with non-targeting control or one of two independent shRNAs targeting DUSP1, prior to intracranial implantation into mice. p-values were calculated using Student's t test. **(J)** Tumor weight following treatment with DUSP1/6 inhibitor in mice subcutaneously implanted with CH157-MN cells was compared following two weeks of treatment with DMSO (black) or BCI (red). Tumor weights were compared using Wilcoxon rank-sum test. Boxplots are represented as the median plus interquartile range. **(K)** Tumor volume following treatment with DUSP1/6 inhibitor in mice subcutaneously implanted with CH157-MN cells was compared following two weeks of treatment with DMSO (black) or BCI (red). Tumor volumes were compared using Wilcoxon rank-sum test. Boxplots are represented as the median plus interquartile range. **(L)** Image of tumors from mice treated with DMSO (top) or BCI (bottom). P-values were calculated by Student's t test for <3 comparisons, or by ANOVA followed by Tukey's honest significant different for 3 comparisons. *p< 0.05, **p<0.005, ***p<0.0005

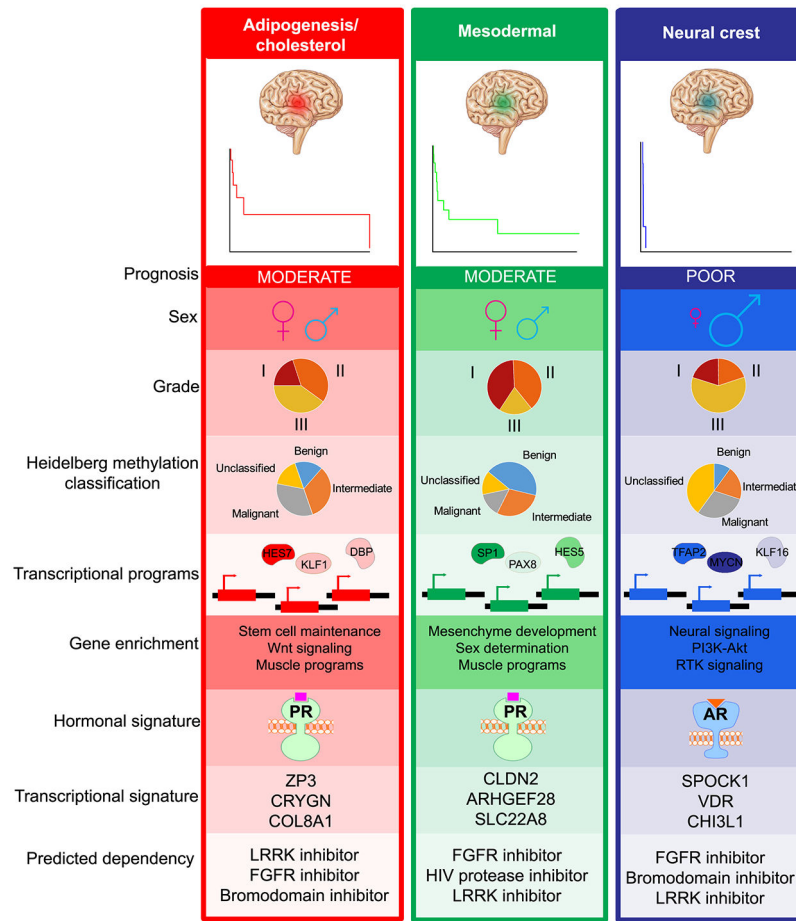


Figure 7.
Summary of enhancer subgroups.